Combustion and Flame 197 (2018) 161–181

Contents lists available at ScienceDirect

Combustion and Flame

journal homepage: www.elsevier.com/locate/combustflame

Downward flame spread along a single pine needle: Numerical modelling

Kambam Naresh[a], Amit Kumar[a,*], Oleg Korobeinichev[b], Andrey Shmakov[b], Ksenia Osipova[b]

[a] Department of Aerospace Engineering, Indian Institute of Technology Madras, India
[b] Institute of Chemical Kinetics and Combustion, Russian Academy of Sciences (Siberian Branch), Russia

ARTICLE INFO

Article history:
Received 15 April 2018
Revised 4 June 2018
Accepted 19 July 2018

Keywords:
Diffusion flame
Pine needle
Downward flame spread
Char oxidation
Thin fuel
Numerical modelling

ABSTRACT

In this work downward flame spread over single pine needle of *Pinus Sibirica* is studied. Pine needles are thin cellulosic charring combustible forest fuel elements. Idealising pine needles to thin cylinders, a 2D axisymmetric numerical model is developed accounting for char formation and char oxidation to investigate the important mechanisms which control the downward spread of flame over a pine needle in normal gravity, atmospheric condition and at various opposed flow conditions. Simultaneous formation of char and pyrolysate during the pyrolysis process was found to significantly reduce the flame spread rate over thin fuel. Presence of char resulted in change in distribution of fuel vapour mass flux above the fuel surface which led to decrease in forward heat feedback to the fuel and hence the flame spread rate. This mechanism is different from char acting as a thermal barrier to heat transfer from the flame in case of thick fuel. Char oxidation had no influence on flame spread rate as char oxidation was found to occur only after passage of flame with the availability of surrounding oxygen diffusing through the hot plume of combustion products. Char oxidation was primarily controlled by oxygen diffusion rate to the charred fuel surface. The flame spread data for quiescent flame spread, and the blow off opposed flow velocity was used to calibrate gas phase kinetics and pyrolysis kinetics. The model predicted flame spread rate variation with opposed flow velocity quite well. The predicted spatial distribution of temperature and species concentration also compared very well with the experimentally determined flame structure.

1. Introduction

The study of fire propagation in forest fuels is important because of the inherent risk of the potential fire hazard. It is imperative to have a better understanding on how flame spreads over forest fuel so as to contribute to the progress in fire safety research. The critical condition for fire propagation depends on the individual fuel element [1] especially thin components like leaves or the foliage. Therefore, studying the combustion and flame spread mechanism of a single pine needle (SPN), which is one of the most combustible components of forest fuel, will help in understanding the mechanism of flame spread over thin charring solid fuels and ground fire spread.

Flame spread over charring fuels has been studied primarily for thick fuels and study of flame spread over thin charring fuels has received comparatively little attention. A flame spread study over a solid fuel slab by Carrier et al. [2] modelled degradation of the fuel into only pyrolysate, and later incorporated char formation along with pyrolysate in the model, [3]. The study [3] showed that the char layer plays a significant role in thermal resistance, heat retention and solid surface emission. In a study by Wichman and Atreya [4] a simplified model of pyrolysis of thick charring materials identified four stages of pyrolysis namely, inert heating, initial pyrolysis, thin char, and thick char. Study showed that the surface temperature controls the volatile production rate at the initial pyrolysis stages (the kinetically controlled regime), while the temperature gradient controls the volatile production rate at the thick char stage (the diffusion-controlled regime). In the numerical studies of Di Blasi et al. [5] for concurrent flame spread and Di Blasi [6] for opposed flame spread, solid fuel is treated as consisting of two components: combustible pyrolysate and non-combustible char. Char formed from pyrolysis of virgin fuel is considered to occupy the initial volume of the virgin fuel. The study in [5] focused on model development for thin charring fuel under concurrent flow conditions and showed a good match of prediction with the experiment. The work in [6] is focused on the influence of

* Corresponding author.
E-mail address: amitk@ae.iitm.ac.in (A. Kumar).

https://doi.org/10.1016/j.combustflame.2018.07.019
0010-2180/

Nomenclature

$\bar{A}_s$	Virgin fuel pre-exponential factor ($=9.8\times10^{6}$ mm/s)
A_s	Non-dimensional virgin fuel pre-exponential factor ($=\bar{A}_s/\bar{U}_R$)
$\bar{A}_{char}$	Char oxidation pre-exponential factor ($=10^{6.8}$ s^{-1})
A_{char}	Non-dimensional char oxidation pre-exponential factor ($=\bar{A}_c/(\bar{U}_R/\bar{L}_R)$)
A_{CS}	Non-dimensional cross-sectional area of the fuel (πr_f^2)
A_{surf}	Non-dimensional surface area per unit length of the fuel ($2\pi r_f$)
B_O	Boltzmann number ($=\rho^* c_p^* \bar{U}_R/(\sigma\ \bar{T}_\infty^3)$)
$\bar{B}_g$	Gas-phase pre-exponential factor ($=1.5\times10^{12}$ mm^3/ (kg-s))
c_p	Non-dimensional gas- phase specific heat ($=\bar{c}_p\ /c_p^*$)
$\bar{c}_p$	Gas- phase specific heat $=\sum_{i=1}^{N}\bar{c}_{p,i}Y_i$
c_p^*	Reference gas- phase specific heat ($=1.38^{3}$ kJ/kgK)
$\bar{c}_{s,v}$	Specific heat of virgin fuel ($\bar{c}_{s,v}=(0.004\overline{T_s}+0.02)\ kJ/kgK$)
$\bar{c}_{char}$	Specific heat of char/ash ($=1.46$ kJ/kgK)
$\bar{c}_s$	Solid- phase specific heat ($=\bar{c}_{s,v}*(\rho_s/\rho_{TO})+\bar{c}_{char}*(\rho_c+\rho_{ash})/\rho_{TO}$)
c_s	Non-dimensional specific heat of solid ($=\bar{c}_s\ /c_p^*$)
Da	Damköhler number ($=\alpha^*\rho^*\bar{B}_g/\bar{U}_R^2$)
D_i	Non-dimensional diffusion coefficient of species i ($\rho D_i/\rho^* D_i^*$) $=(T/T^*)^{0.7}$ (Sutherland law)
$\bar{E}_g$	Gas- phase activation energy ($=1.25\times10^5$ kJ/kmol)
E_g	Non-dimensional gas- phase activation energy ($=\bar{E}_g/(\bar{R}_u\ \bar{T}_\infty)$)
$\bar{E}_s$	Solid -phase activation energy ($=10.9\times10^4$ kJ/kmol)
E_s	Non-dimensional solid phase activation energy ($=\bar{E}_s/(\bar{R}_u\ \bar{T}_\infty)$)
$\bar{E}_{char}$	Char oxidation activation energy ($=1.16\times10^5$ kJ/kmol)
E_{char}	Non-dimensional char oxidation activation energy ($=\bar{E}_{char}/(\bar{R}_u\ \bar{T}_\infty)$)
f_i	Stoichiometric mass ratio of species i / fuel in gas phase
F_i	Stoichiometric ratio of species i/char in char oxidation reaction
$\bar{g}$	Gravitational acceleration
$\bar{g}_e$	Gravitational acceleration on the surface of earth ($\bar{g}_e=9.81$ m/s^2)
g	Non-dimensional gravitational acceleration ($\bar{g}/\bar{g}_e$)
G	Total incident radiation
h_i	Non-dimensional enthalpy of species i $=(\bar{h}_i^o+\int_{\bar{T}_o=298\ K}^{\bar{T}}\bar{c}_{p,i}d\bar{T})/c_p^*\bar{T}_\infty$
$\Delta\bar{H}_R^o$	Heat of combustion ($=16.9\times10^3$ kJ/kg)
ΔH_R^o	Non-dimensional heat of combustion ($=\Delta\bar{H}_R^o/(c_p^*\bar{T}_\infty)=40.9$)
I	Intensity of gas radiation
I_b	Blackbody intensity at local temperature
k	Non-dimensional gas thermal conductivity ($=\bar{k}\ /k^*$)
k^*	Reference gas thermal conductivity ($=4.6\times10^{-6}$ kJ/(m-s-K))
$\bar{k}_s$	Thermal conductivity of solid fuel ($=1.73\times10^{-5}$ kJ/(m-s-K))
k_s	Non-dimensional solid thermal conductivity ($=\bar{k}_s/k^*$)
K	Absorption coefficient of the medium
L	Non-dimensional latent heat of pyrolysis ($=0$)
Le_i	Lewis number of species i ($Le_F=1, Le_{O2}=1.11, Le_{CO2}=1.39,\ Le_{H2O}=0.83,$)
$\bar{L}_R$	Reference length (gas-phase thermal length, ($\alpha^*/\bar{U}_R$)
$\overline{\dot{m}''}_s$	Mass flux from solid ($=\bar{A}_s\bar{\rho}_s\exp(-E_s/T_s)$)
$\dot{m}_s''$	Non-dimensional mass flux from solid ($=\overline{\dot{m}''}_s\ /(\rho^*\bar{U}_R)$)
$\dot{m}_c'''$	Non-dimensional mass of carbon consumed per unit volume ($=\overline{\dot{m}_c'''}\ /\ (\rho^*\bar{U}_R/\bar{L}_R)$)
$\dot{m}_o'''$	Non-dimensional mass of oxygen consumed per unit volume ($=\overline{\dot{m}_o'''}\ /\ (\rho^*\bar{U}_R/\bar{L}_R)$)
p	Non-dimensional pressure ($=\ (\bar{p}-\bar{p}_\infty)/(\rho^*\bar{U}_R^2)$)
$\bar{p}_\infty$	Ambient pressure ($=1$ atm)
$\bar{q}_r$	Gas radiation heat flux
q_c''	Non-dimensional conduction heat flux from gas to fuel surface ($=\overline{q_c''}/c_p^*\rho^*\bar{U}_R$)
q_r''	Net radiation heat flux at the fuel surface ($=\ \bar{q}_r''/\sigma\bar{T}_\infty^4$)
$\bar{q}_{char}$	Heat release due to char oxidation per unit mass ($=28\times10^3$ kJ/kg)
q_{char}	Heat release due to char oxidation per unit mass ($=\bar{q}_{char}/(c_p^*\bar{T}_\infty)$)
q_r^{r+}, q_r^{r-}	Positive and negative component of q_r in r-direction
q_r^{x+}, q_r^{x-}	Positive and negative component of q_r in x-direction
r	Non-dimensional r-coordinate ($\bar{r}/\bar{L}_R$)
$\bar{r}_f$	Radius of the fuel ($=0.4$ mm)
r_f	Non-dimensional radius of the fuel ($=\bar{r}_f/\ \bar{L}_R$)
$\bar{R}_u$	Universal gas constant ($=8.305$ kJ/(kmol-K))
Re	Reynolds number ($=\rho^*\bar{U}_R\bar{L}_R/\mu^*$)
R^*	Universal gas constant (8.314 kJ/mol-K)
T^*	Reference temperature (1250 K)
T	Non-dimensional gas-phase temperature ($\bar{T}/T^*$)
T_L	Non-dimensional temperature at which latent heat is given
T_s	Non-dimensional solid-phase temperature ($=\overline{T_s}/\ \bar{T}_\infty$)
$\bar{T}_\infty$	Ambient temperature ($=300$ K)
t	Non dimensional time ($=\bar{t}/t_R$)
t_R	Reference time ($=\alpha^*/\bar{U}_R^2$)
$\bar{u}$	Velocity in x-direction
u	Non-dimensional velocity in x-direction ($=\bar{u}/\bar{U}_R$)
$\bar{U}_B$	Buoyant reference velocity $[g_R\beta_R(T_\infty-T_F)\alpha^*]^{1/3}$
$\bar{U}_R$	Reference velocity ($=\max(\bar{U}_\infty+\bar{U}_B,\ 50$ mm/s)
$\bar{U}_\infty$	Forced flow velocity
$\bar{v}$	Velocity in r-direction
v	Non-dimensional velocity in r-direction ($=\bar{v}/\bar{U}_R$)
v_w	Non-dimensional velocity in r-direction at the solid surface
$\vec{V}$	Non-dimensional velocity vector ($=u\ \hat{i}+v\ \hat{j}$)
$\Delta\forall$	Non-dimensional elementary volume of pine needle
V_f	Dimensional flame spread rate
v_f	Non-dimensional flame spread rate ($=\ V_f/\bar{U}_R$)
x	Non-dimensional x-coordinate ($\bar{x}/\bar{L}_R$)
Y_i	Mass fraction of species i (i = F, O_2, CO_2, H_2O)
Y_{pyro}	Mass fraction of pyrolysate ($=0.62$)
Y_c	Mass fraction of carbon present in char ($=0.342$)
Y_{ash}	Mass fraction of ash present in char ($=0.038$)
Y_{char}	Mass fraction of char ($=Y_c+Y_{ash}$)

Greek Symbols

α^*	Reference gas thermal diffusivity (2.13×10^{-4} m^2/s)
β	Extinction coefficient ($= k + \sigma_s$)
σ_s	Scattering coefficient
Φ	Scattering phase function
μ	Non-dimensional gas dynamic viscosity ($= \bar{\mu} \ / \ \mu^*$)
μ^*	gas viscosity (4.1×10^{-5} kg/m/s)
$\dot{\omega}_i'''$	Sink/source term in gas-phase reaction ($= f_i \dot{\omega}_F''' = f_i Da \rho^2 Y_F Y_{O2} \exp(-E_g/T)$)
$\dot{\omega}_{char\ oxid}'''$	Rate of char oxidation ($= A_c \rho_c Y_{O2} \exp(-E_c/R_u T)$)
ρ	Non-dimensional gas density
ρ^*	Reference gas density (0.275 kg/m^3)
ρ_{char}	Non-dimensional char density ($= \bar{\rho}_{char} \ / \rho^* = \ \rho_c + \rho_{ash}$)
ρ_c	Non-dimensional carbon density ($= \ \bar{\rho}_c \ / \rho^*$) in the char
ρ_{ash}	Non-dimensional ash density ($= \bar{\rho}_{ash} \ / \rho^*$)
ρ_s	Non-dimensional density of unburnt solid fuel ($= \bar{\rho}_s \ / \rho^*$)
ρ_T	Non-dimensional total density of the fuel ($= \bar{\rho}_T / \rho^* = \ \rho_s + \rho_{char}$)
$\bar{\rho}_{TO}$	Initial total density ($= 600$ kg/m^3)
ρ_{TO}	Non-dimensional initial total density of the fresh fuel ($= \bar{\rho}_{TO} / \rho^*$)
σ	Stefan-Boltzmann constant (5.678×10^{-8} J/m^2/s/K^4)
ξ, μ, η	Direction cosines in x, r and θ directions
ε	Solid emittance
α	Solid absorptance

Subscripts

B	*Buoyant*
b	*Black body*
c	*Carbon*
F	*Fuel or flame*
g	*Gas phase*
i	*Species i*
R	*Reference*
s	*Solid phase*
w	*Value at wall*
∞	*Value at far field*

Superscripts

*	*Evaluated at T**
-	*Dimensional quantity*

fuel thickness on opposed flow flame spread. The work reported three main regimes of opposed flow flame spread depending on fuel thickness. The dominant mechanism of heat feedback to the unburnt fuel was determined to be conduction from gas phase. It was predicted that as the solid fuel thickness increases, the solid phase conduction becomes important and can reach up to 50% of the total heat feedback mechanism. In both [5] and [6] role of char on the flame spread process was not explicitly explored, especially for thin fuels. In an analytical model for flame spread for thick charring fuel proposed by Atreya [7] the char layer that is formed is considered to insulate the fuel surface. It thickens with time and gives rise to a two-phase moving boundary in the solid. The consideration of insulating char layer is reported to have significant influence on the flame spread rate, as the char layer thickens flame spread rate decreases. The study on the heat and mass transfer processes during wood pyrolysis by Park et al. [8] considered the fuel to decompose into three major products: tar, gas and an intermediate solid by three parallel endothermic reactions and then an exothermic reaction wherein the intermediate solid decomposes to char, and tar decomposes to gas and char. The key finding from this study was that elevated pressure develops inside the fuel and causes the sample to split during pyrolysis. In the ignition transient studies by Nakamura et al. [9,10] char oxidation sub-model was included in the model. However, the role of char oxidation and its phenomena were not explored.

It is clear from the above works that role of char in thin fuels has not been explicitly explored. Therefore, the purpose of this study is to numerically model char oxidation and other important mechanisms that govern downward flame progression along charring combustible materials, here represented by a single pine needle. A axisymmetric computational model is developed where the shape of the pine needle is taken as a thin cylindrical segment.

Experimental work [11] is appreciated for the fact that only limited data are available on flame spread over a pine needle. Experimental and numerical studies on cylindrical fuel were conducted by many researchers [12–18] in the past. The main objective of these studies was to study the effect of gas flow velocity, ambient oxygen concentration, pressure, gravity, fuel thickness on flame spread rate but no char formation was considered. Therefore, in a collaborative effort an experimental study was taken up recently by the Korobeinichev et al. [19] on downward flame spread over pine needle segments. This study has been crucial for the present work to provide not only global data like flame spread rate under different opposed flow conditions but also flame structure details and consistent fuel properties required for numerical modelling. The experiments in [19] are summarized next.

2. Experiments

The details of the experiments on downward flame spread over a single pine needle have been reported in a recent work by the authors [19]. Here only a summary is presented for adequate background and completeness of information required for numerical modelling. Experiments of downward flame spread over a single pine needle were carried out for straight pine-needle (*Pinus Sibirica*) segments of nearly identical size. The typical pine needle in the experiment was about 20–25 mm long and had a cross section of about 1 mm x 0. 6 mm. A schematic of a pine needle with locations of temperature measurement are illustrated in Fig. 1.

The figure on the right side shows an instantaneous image of the downward spreading flame in a typical experiment. The pine needles were dried in an oven at the temperature of 60 °C for a period of 24 hours. This ensured that the moisture content in the pine needle was nearly the same, typically between 7.8% and 9.4%. A thin Pt–Pt + 10% Rh thermocouple (T1), 0.05 mm in diameter, was placed inside the pine needle at the midpoint of its length and in the middle of its cross section. The pine needle was positioned vertically by the leads of this thermocouple. The gas-phase temperature was measured with a 0.02-mm Pt–Pt + 10% Rh thermocouple (T2). The junction of T2 was placed near the mid length of the pine needle and at a distance from the surface of the pine needle which varied from 0.2 mm to 7 mm. The temperature was measured at a frequency of 1 kHz and with an accuracy of ± 5 K. The appendix shows two figures from [19]. Figure A1 of Appendix (Fig. 6 of [19]) shows typical measured temperatures T1 (at 0.2 mm from pine needle surface) and T2 along the length of the pine needle. The figure is obtained by translating temperature data measured in time to data varying along the pine needle length by multiplying time with flame spread rate. Also shown on the figure are numbers 1–7 which indicate turning on/off of LED lamp at various instants of time. The spreading flame positions at these instances are shown in Fig. A2 (Fig. 7 of [19]). In addition to micro thermocouple measurements, mass spectrometry with microprobe

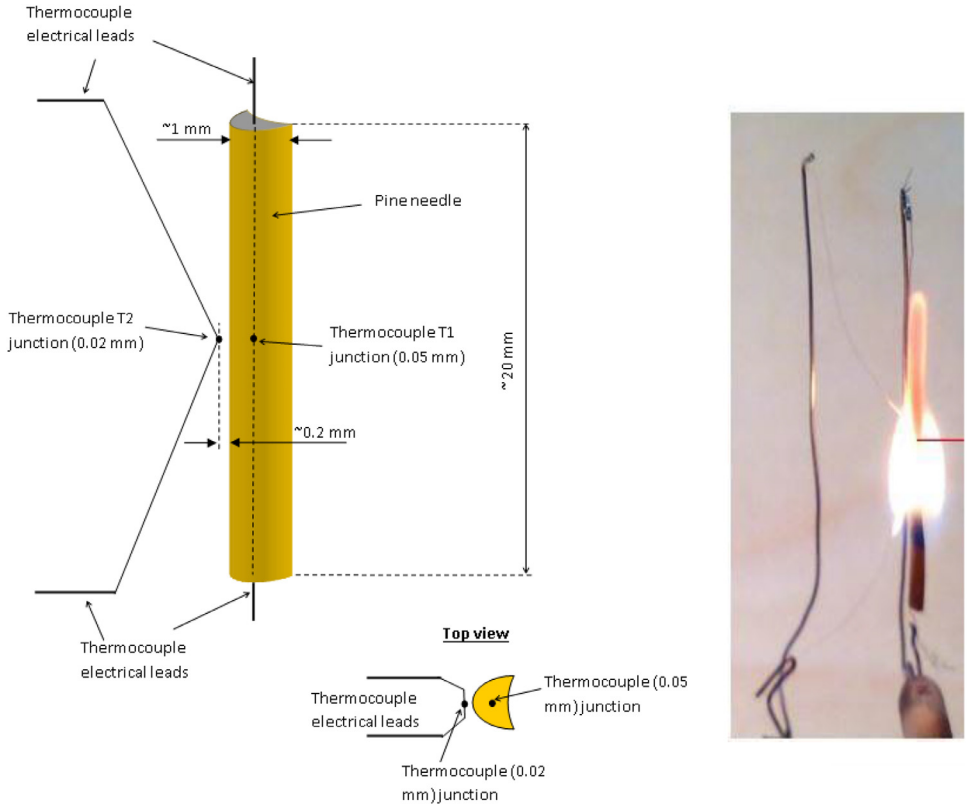

Fig. 1. Schematic of pine needle and snapshot of downward spreading flame over single pine needle from the experiment.

sampling (with relative accuracy error of about ± 5-10%) was used to measure the concentration profiles of O_2 and the main combustion products (CO_2, CO, H_2O). The microprobe was positioned in the middle of the pine needle along its length, and at distances from the pine needle surface which varied from 1 mm to 7 mm. The microprobe sampling method was also used to measure temperature distribution for downward flame spread along the needle length. The downward flame spread rate was also measured for several counter-flow air velocities up to the point of extinction to obtain dependence of the flame spread rate on counter-flow velocity.

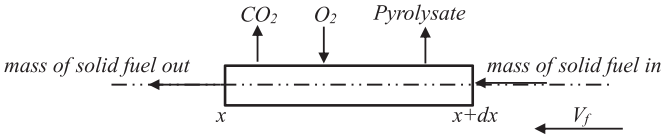

Fig. 2. Schematic showing mass balance about an elemental control volume drawn about a segment of the pine needle.

3. Numerical modelling

Modelling the pyrolysis and combustion processes in flame spreading over a single pine needle is a complex task. Complexities may include non-simple geometries, heterogeneous composition, heat and mass transport, fuel pyrolysis processes and kinetics and transport process in the gas phase. Numerical models to predict flame spread phenomena have evolved over nearly five decades. As mentioned before, the numerical models have progressively included more sub-models to explain subtle details of the flame spread mechanism. However, some simplifying assumptions were still essential even in contemporary numerical models.

The key assumptions in the present numerical model are summarized next. First, the pine needle was modelled as a cylindrical fuel with a uniform diameter. The 1 mm × 0.6 mm cross section of pine needle was approximated by a cylindrical cross section of diameter 0.8 mm. The downward flame spread was seen to achieve a steady value within 1–2 s after ignition. Therefore, the flame spread rate was assumed to be quasi-steady in the flame fixed coordinate system and the flame anchoring position is located at the middle of the pine needle. Figure 2 shows mass balance about an elemental control volume, Fig. 3a shows a schematic of the pine needle model, and Fig. 3b shows the computational domain, grid structure and flame anchoring location (x = 0).The fuel was assumed to be both aerodynamically thin and thermally thin. Here aerodynamically thin implies that aerodynamics effects of pine needle thickness at the leading and trailing edges are neglected.

The pine needle surface was assumed to be flush with the gas domain at leading and trailing edges. Thermally thin implies that no temperature gradient exists radially inside the solid fuel. This condition holds true when the thermal diffusion time is small, compared to the time for the flame to spread over the characteristic length scale. The flow velocities are small (< 1–2 m/s), so the flow is assumed to be laminar. The fuel in the pine needle is assumed to comprise combustible cellulosic pyrolysate vapours, carbonaceous char and inert ash in known proportions. The decomposition of fuel is assumed to take place in two steps. In the first step, virgin fuel decomposes to form volatiles or the pyrolysate and solid carbonaceous residue char. This carbonaceous solid is assumed to comprise pure carbon and ash. In the second step, the carbon in the char oxidises to form carbon dioxide, and ash is left over as

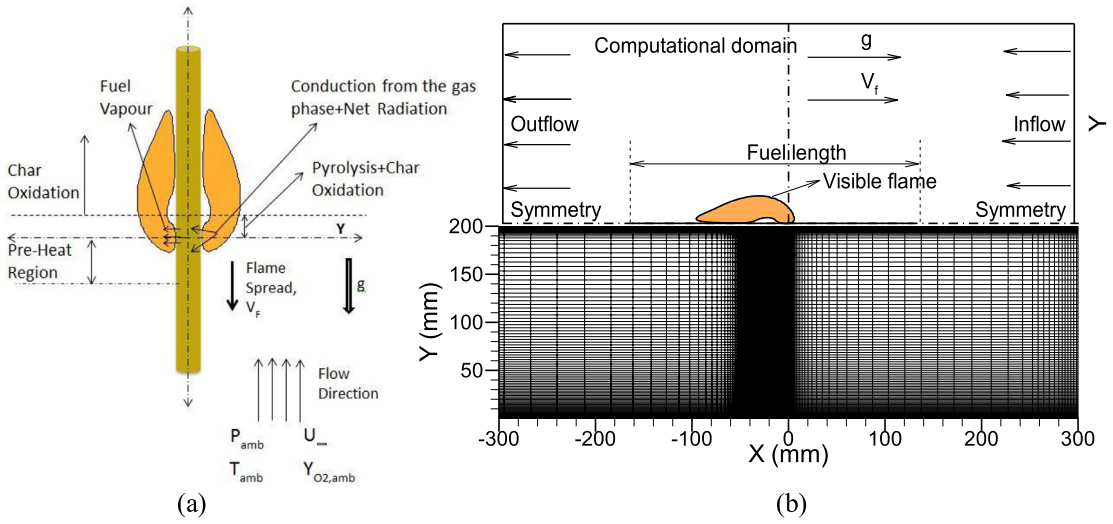

Fig. 3. (a) Schematic of pine needle model, (b) computational domain, boundaries and grid structure.

solid residue.

$$Virgin\ fuel \rightarrow Pyrolysate + Char(carbon + ash)$$
$$Char(C + ash) + (O_2 + 3.76N_2) \rightarrow CO_2 + 3.76N_2 + ash \quad (1)$$

A one-step, second-order global gas-phase reaction between fuel vapour and oxygen, obeying Arrhenius type kinetics is assumed. The ideal gas law holds for all the component gases. Specific heats are functions of temperature for each species and are obtained from standard reference. The transport properties are modelled following [20]. Solid fuel pyrolysis follows a first-order, one-step Arrhenius kinetics. The gas-phase thermal radiation is assumed to come from carbon dioxide and water vapour only. The solid radiation is assumed to be diffuse.

The pyrolysate fuel is cellulose material with chemical formula of $C_6H_{10}O_5$. The stoichiometric combustion of fuel in air can thus be written as:

$$C_6H_{10}O_5 + 6(O_2 + 3.76N_2) \rightarrow 6CO_2 + 5H_2O + 22.56N_2 \quad (2)$$

For the above one-step cellulose and air stoichiometric reaction, the stoichiometric mass ratios are ($f_F = -1$, $f_{O2} = -1.1852$, $f_{CO2} = 1.6296$, $f_{H2O} = 0.5556$, $f_{N2} = 3.901$)

Oxidation of carbon in the char by air is described by reaction

$$C + (O_2 + 3.76N_2) \rightarrow CO_2 + 3.76N_2 \quad (3)$$

The stoichiometric mass ratios for char oxidation are as $F_C = -1$, $F_{O2} = -2.66$, $F_{CO2} = 3.66$

The rate of char oxidation is controlled by sequential or parallel processes of boundary layer diffusion, chemical reaction and pore diffusion. Several investigators [21,22] have postulated the existence of three different regimes in which one or more different processes control the overall reaction rate. In the literature the models for char oxidation are broadly classified into two main categories, namely, global models and intrinsic models [23]. In the intrinsic models, the active surface area and the oxygen concentration within the char are taken into account, while in the global char oxidation model, pore diffusion is neglected and the char oxidation rate is controlled either by reaction kinetics or oxygen diffusion rate at the surface. The pine needle being a thin charring fuel, a global char oxidation model is sufficient (and simpler) to account for essential physico-chemical process involved compared with complex intrinsic model.

The present 2D axisymmetric numerical code is developed from an existing 2D planar opposed-flow flame spread model for thin fuels [24–26] which has been used successfully to predict various aspects of flame spread over thin fuels. The governing equations and boundary conditions in the gas phase and the solid phase are detailed next.

4. Gas-phase model

The gas-phase model consists of governing equations of full Navier–Stokes equations for laminar flow, along with the conservation equations of mass, energy and species in cylindrical coordinates. The species equations are for fuel vapor, oxygen, carbon dioxide and water vapor. As mentioned previously, a one-step, second-order finite-rate Arrhenius reaction between fuel vapor and oxygen is assumed. The governing equations are presented in a non-dimensional form. The non-dimensional gas phase equations are summarized below.

4.1. Continuity equation

$$\frac{\partial \rho}{\partial t} + \frac{\partial \rho u}{\partial x} + \frac{\partial \rho v}{\partial r} + \frac{\rho v}{r} = 0 \quad (4)$$

4.2. Axial or x-momentum equation

$$\frac{\partial(\rho u)}{\partial t} + \nabla\left[\rho u\vec{\boldsymbol{V}} - \frac{\mu}{Re}\nabla u\right] = -\frac{\partial p}{\partial x} + \frac{1}{Re}\left[\frac{\partial}{\partial x}\left(\frac{1}{3}\mu\frac{\partial u}{\partial x} - \frac{2\mu}{3}\frac{\partial v}{\partial r}\right)\right] + \frac{1}{Re}\frac{\partial}{\partial r}\left(\mu\frac{\partial v}{\partial x}\right) + \frac{1}{Re}\left[\frac{1}{r}\left(\frac{\mu}{3}\frac{\partial v}{\partial x}\right)\right] + \left(\frac{U_B}{U_R}\right)^3\frac{(\rho-\rho_\infty)}{(\rho_s-\rho_\infty)}g - \left(\frac{dv_f}{dt}\right)\frac{(\rho-\rho_\infty)}{(\rho_f-\rho_\infty)} \quad (5)$$

4.3. Radial or r-momentum equation

$$\frac{\partial(\rho v)}{\partial t} + \nabla\left[\rho v\vec{\boldsymbol{V}} - \frac{\mu}{Re}\nabla v\right] = -\frac{\partial p}{\partial r} + \frac{1}{Re}\left[\frac{\partial}{\partial x}\left(\mu\frac{\partial u}{\partial r}\right)\right] + \frac{1}{Re}\left[\frac{\partial}{\partial r}\left(\frac{\mu}{3}\frac{\partial v}{\partial r} - \frac{2}{3}\mu\frac{\partial u}{\partial x}\right)\right] + \frac{1}{Re}\left[\frac{1}{r}\left(\frac{1}{3}\mu\frac{\partial v}{\partial r} - \frac{4}{3}\mu\frac{v}{r}\right)\right] \quad (6)$$

Where,

$v_f = \frac{V_f}{\bar{U}_R}$ = non-dimensional flame spread rate
V_f = dimensional flame spread rate
$\bar{U}_R$ = reference velocity
$Re = \rho^* \bar{U}_R \bar{L}_R / \mu^*$ = Reynolds number

4.4. Species equation

$$\frac{\partial(\rho Y_i)}{\partial t} + \frac{\partial}{\partial x}\left(\rho Y_i u - \left(\frac{1}{Le_i}\right) D_i \frac{\partial(\rho Y_i)}{\partial x}\right) + \frac{\partial}{\partial r}\left(\rho Y_i v - \left(\frac{1}{Le_i}\right) D_i \frac{\partial(\rho Y_i)}{\partial r}\right) = \left(\frac{1}{Le_i}\right)\frac{1}{r} D_i \frac{\partial(\rho Y_i)}{\partial r} - \frac{\rho v Y_i}{r} + \dot{\omega}_i''' \quad (7)$$

Where

$i = F, O_2, CO_2, H_2O, N_2$
Y_i = mass fraction of species i
D_i = diffusion coefficient of species i
$\dot{\omega}_i'''$ = sink/source term in gas-phase reaction
$= f_i \dot{\omega}_F''' = f_i Da \rho^2 Y_F Y_{O2} \exp(-E_g/T))$

where,

f_i is the stoichiometric mass ratio of species i and fuel

Da = Damkohler number = characteristic flow time/characteristic reaction time

$$= \frac{\bar{L}_R/\bar{U}_R}{\rho^*/\rho^{*2}\bar{B}_g} = \frac{\bar{B}_g \rho^* \bar{L}_R}{\bar{U}_R} = \frac{\alpha^* \rho^* \bar{B}_g}{\bar{U}_R^2}$$

Here, $\bar{L}_R$ is reference length, α^*, ρ^* are thermal diffusivity and density of the gas phase at reference temperature $T^*(1250\,K)$ respectively and $\bar{B}_g$ is gas phase pre-exponential factor.

Le_i = Lewis number of specie 'i' = diffusion time/(convection/conduction time)

$$= \frac{\overline{L_R^2}/D_i^*}{\bar{L}_R/\bar{U}_R} = \frac{\overline{L_R^2}/D_i^*}{\overline{L_R^2}/\alpha^*} = \frac{\alpha^*}{D_i^*}$$

$(Le_F = 1, Le_{O2} = 1.11, Le_{CO2} = 1.39, Le_{H2O} = 0.83,\ Le_{N2} = 1)$

4.5. Energy equation

$$\frac{\partial(\rho c_p T)}{\partial t} + \frac{\partial}{\partial x}\left(\rho c_p u T - k\frac{\partial T}{\partial x}\right) + \frac{\partial}{\partial r}\left(\rho c_p v T - k\frac{\partial T}{\partial r}\right) = \sum_{i=1}^{N}\left(\frac{1}{Le_i}\right)\rho D_i c_{pi} \vec{\nabla} Y_i \vec{\nabla} T - \sum_{i=1}^{N} h_i \dot{\omega}_i''' + \frac{1}{r} k \frac{\partial T}{\partial r} + \vec{\nabla} c_p \vec{\nabla} T\left(\frac{k}{c_p}\right) - \left(\frac{1}{B_0}\right)\vec{\nabla}.\vec{q}_r \quad (8)$$

where

c_{pi} is non-dimensional specific heat of species i.
c_p is non-dimensional gas- phase specific heat and it can be calculated as $\sum_{i=1}^{N} c_{pi} Y_i$
k is non-dimensional gas phase thermal conductivity.
h_i non-dimensional enthalpy of species i = $(\bar{h}_i^o + \int_{\bar{T}_o=298\ K}^{\bar{T}} \bar{c}_{p,i} d\bar{T})/c_p^* \bar{T}_\infty$
B_0 = Boltzman number
$= \frac{\rho^* c_p^* \bar{U}_R}{\sigma \bar{T}_\infty^3}$

The term $\nabla.\vec{q}_r$ is the divergence of radiation heat flux which accounts for energy exchange due to presence of radiatively participating media.

5. Gas-phase boundary conditions

The elliptic nature of the governing equations requires boundary conditions to be specified at all boundaries. These boundary conditions are listed below.

Inlet or upstream ($X = x_{max}$)

$$u = \frac{\bar{U}_\infty - V_f}{\bar{U}_R},\ v = 0 \quad (9.1)$$

$$T = 1,\quad Y_{O2} = Y_{O2,inlet}, Y_i = 0 (i = F, CO_2, H_2O) \quad (9.2)$$

Exit or downstream ($X = x_{min}$)

$$\frac{\partial u}{\partial x} = 0\ ,\ \frac{\partial v}{\partial x} = 0 \quad (10.1)$$

$$\frac{\partial T}{\partial x} = 0,\ \frac{\partial Y_i}{\partial x} = 0\ (i = O_2, F, CO_2, H_2O\ ) \quad (10.2)$$

Top ($Y = y_{max}$, Open domain)

$$u = \frac{\bar{U}_\infty - V_f}{\bar{U}_R} \quad \frac{\partial v}{\partial y} = 0 \quad (11.1)$$

$$T = 1 \quad \frac{\partial Y_i}{\partial y} = 0 \quad (i = O_2, F, CO_2, H_2O) \quad (11.2)$$

Fuel surface ($Y = 0$)

$$u = -\frac{V_f}{\bar{U}_R} \quad v = v_w \quad T = T_s \quad (12)$$

where,

v_w is the wall velocity at the fuel surface and it is calculated as follows:

v_w = Mass flux at the fuel surface/density of the gas phase at the interface

$\dot{m}''/\rho$

$\bar{U}_\infty$ is opposed flow velocity and T_s is non-dimensional gas-solid interface temperature/solid temperature.

5.1. Fuel

In the following equations, + and − sign represents upper side (gas) and lower side (fuel) of a gas-fuel interface respectively

when char present

$$\dot{m}'' Y_{F,w+} - (\rho D_F / Le_F) * (\partial Y_F / \partial r)_w = \dot{m}'' Y_{F,w-} \quad (13.1)$$

In the above equation, the term on the LHS represents the combined species mass flux due to convection and diffusion at the upper side of the interface, while the RHS represents species mass flux at the lower side of the gas-solid interface. Here, $\dot{m}'' Y_{F,w-} = Y_{pyro} \dot{m}_s''$, which is the mass flux of the pyrolysate and $\dot{m}_s''$ is calculated as $\dot{m}_s'' = A_s \rho_s \exp(-E_s/T_s)$ using first order pyrolysis law.

when char not present,

$Y_{F,w-} = 1$, and mass fraction of pyrolysate $Y_{pyro} = 1$

Eq. (13.1) reduces to

$$\dot{m}'' Y_{F,w+} - (\rho D_F / Le_F) * (\partial Y_F / \partial r)_{w+} = \dot{m}'' \quad (13.2)$$

where

$\dot{m}'' = \dot{m}_s''$

5.2. Other species

when char present

no char oxidation

$$\dot{m}''Y_{i,w+} - (\rho D_i / Le_i) * (\partial Y_i/\partial r)_{w+} = \dot{m}''Y_{i,w-} = 0 \quad (14.1)$$

$(i = O_2, CO_2, H_2O)$

In the above equation, $Y_{i,w-} = 0$

char oxidation

$$\dot{m}''Y_{i,w+} - \left(\frac{\rho D_i}{Le_i}\right) * (\partial Y_i/\partial r)_{w+} = \dot{m}''Y_{i,w-} = 0 \quad (14.2)$$

$(i = H_2O)$

$$\dot{m}''Y_{i,w+} - \left(\frac{\rho D_i}{Le_i}\right) * (\partial Y_i/\partial r)_{w+} = \dot{m}''Y_{i,w-} \quad (14.3)$$

$(i = CO_2,\ O_2)$

In the limit of diffusion controlled char oxidation

Oxygen:

$$Y_{O_2,w+} = 0,\ Y_{O_2,w-} = 0 \quad (14.3a)$$

and oxygen mass flux at the fuel surface can be determined as $(\rho D_{o_2} / Le_{o_2}) * (\partial Y_{o_2}/\partial r)_{w+}$ and hence we can also determine *carbon dioxide mass flux as follows:*

Carbon dioxide:

$$\dot{m}''Y_{CO_2,w-} = (FCO_2/FO_2) * (\rho D_{o_2} / Le_{o_2}) * (\partial Y_{o_2}/\partial r)_{w+} \quad (14.3b)$$

In the limit of kinetic controlled char oxidation

Oxygen:

$$\dot{m}''Y_{O_2,W-}A_{surf} = FO_2 * \dot{\omega}'''_{char\ oxid} * \Delta\forall \quad (14.3c)$$

A_{surf} and $\Delta\forall$ are elemental surface area and volume of the pine needle fuel

$\dot{\omega}'''_{char\ oxid}$ = Rate of char oxidation $(= A_c \rho_c Y_{O2} \exp(-E_c/R_u T))$

Carbon dioxide:

$$\dot{m}''Y_{CO_2,W-}A_{surf} = FCO_2 * \dot{\omega}'''_{char\ oxid} * \Delta\forall \quad (14.3d)$$

here, $\dot{m}'' = \dot{m}''_{CO_2} + \dot{m}''_{O_2} + Y_{pyro}\dot{m}''_s$

5.3. When char not present

$$\dot{m}''Y_{i,w+} = (\rho D_i / Le_i) * (\partial Y_i/\partial r)_{w+} (i = O_2, CO_2, H_2O) \quad (15)$$

Symmetry condition on segment that is not fuel surface (Y = 0)

$$\frac{\partial u}{\partial r} = 0\ ,\ \ v = 0 \quad (16.1)$$

$$\frac{\partial T}{\partial r} = 0,\ \ \frac{\partial Y_i}{\partial r} = 0\ (i = O_2, F, CO_2, H_2O) \quad (16.2)$$

6. The solid phase model

6.1. Solid phase mass conservation equation

$$\frac{\partial \rho_T}{\partial t} - v_f \frac{\partial \rho_T}{\partial x} = -\left(\frac{A_{surf}}{\Delta\forall} Y_{pyro}\dot{m}_s'' + \dot{m}_c'''\right) = \frac{2}{r_f} Y_{pyro}\dot{m}_s'' + \dot{m}_c''' \quad (17.1)$$

where $\frac{A_{surf}}{\Delta\forall} = \frac{2\pi r_f \Delta x}{\pi r_f^2 \Delta x} = \frac{2}{r_f}$ and $\rho_T = \rho_s + \rho_c + \rho_{ash}$

$\dot{m}'''_{char}$ = mass rate of char consumed per unit volume

= mass rate of carbon oxidation + ash production = $\dot{m}'''_c + \dot{m}'''_{ash}$

$\dot{m}'''_c$ = mass rate of carbon per unit volume leaving the fuel as carbon dioxide

$= Y_C * \ \dot{m}'''_{char} / \ (Y_{ash} + Y_c)$

$\dot{m}'''_{ash}$ = mass rate of ash produced as a result of char oxidation

$= Y_{ash} * \ \dot{m}'''_{char} / \ (Y_{ash} + Y_c)$

Here, char is considered to comprise of carbon and ash

The first term on the right hand side of Eq. (17.1) is the mass rate of pyrolysate formed per unit volume from pyrolysis of virgin fuel. The second term is the mass rate of carbon per unit volume leaving the fuel as carbon dioxide. As mentioned before, ash is assumed to be a component in carbonaceous char. The mass rate of conversion of carbon in the char to carbon dioxide is related to the mass rate of oxygen consumption through carbon oxidation reaction stoichiometry.

$$\frac{Y_c}{(Y_c + Y_{ash})}\dot{m}'''_{char} = \left(\frac{1}{FO_2}\right) * \dot{m}'''_{O_2}$$

The oxygen mass consumption rate can be obtained as $\dot{m}'''_{O_2} = FO_2\ \dot{\omega}'''_{char\ oxid}$ if char oxidation is kinetically controlled or as $\dot{m}'''_{O_2} = (\rho_g D_{O_2})(\partial Y_{O_2}/\partial r)_w * A_{surf}/\Delta\forall$ if the process is diffusion controlled. The slower of the two processes controls the overall char oxidation process.

6.2. Mass conservation equation for char

$$\frac{\partial \rho_{char}}{\partial t} - v_f \frac{\partial \rho_{char}}{\partial x} = \frac{2}{r_f}(Y_{ash} + Y_c)\dot{m}_s'' - \dot{m}'''_{char} \quad (17.2)$$

6.3. Mass conservation equation for ash

$$\frac{\partial \rho_{ash}}{\partial t} - v_f \frac{\partial \rho_{ash}}{\partial x} = \frac{Y_{ash}}{(Y_{ash} + Y_c)}\ \dot{m}'''_{char} \quad (17.3)$$

Subtracting equations of conservation of char and ash from the solid phase mass conservation Eq. (17.1), a conservation equation for pyrolysate can be obtained.

$$\frac{\partial \rho_s}{\partial t} - v_f \frac{\partial \rho_s}{\partial x} = -\frac{2}{r_f}\dot{m}_s'' \quad (17.4)$$

In the absence of char $\rho_T = \rho_s$, and the mass conservation equation for the solid fuel reduces simply to the equation for conservation of pyrolysate shown above.

6.4. Energy conservation equation

$$\rho_T \frac{\partial c_s T_s}{\partial t} - \rho_T v_f \frac{\partial c_s T_s}{\partial x} = \frac{2}{r_f}\left(q_c'' + \frac{q_r''}{Bo}\right) + \frac{\partial}{\partial x}\left(-k_s \frac{\partial T}{\partial x}\right) + \dot{m}'''_c q_{char} - \dot{m}'''_c c_s T_s - \frac{2}{r_f}\dot{m}_s'' c_s \times ((1-c)T_l - L + T_s(c - Y_{pyro})) \quad (17.5)$$

In the above equation, the first term in the RHS, q_c'' is the conduction heat flux from the gas phase to the solid, the second term q_r'' is the net radiation heat flux from the flame to the solid fuel, the third term is the heat conduction term along the fuel axis, and the fourth term, q_{char} is the energy release due to char oxidation. The last term on the right-hand side is the heat of pyrolysis, L is the latent heat which is taken as zero in case of a pine needle, T_l is the temperature at which the latent is given and c is c_p/c_s. When char is not present, the source term of heat released due to char combustion is omitted from the equation.

7. Solid phase boundary conditions

The boundary conditions for the solid phase governing equations are prescribed fuel thickness and surface temperature at the fuel leading edge upstream of the flame at $(x = x_0)$

i.e at $x = x_0$ (*leading edge of fuel sample upstrem of flame*)

$T_s = 1,\ \rho_s = \rho_{s0},\ \rho_{char} = 0$ *and* $\rho_{ash} = 0$

8. Radiation transport

In addition to the solid and gas equations, the only other quantity that needs to be determined is the radiation heat flux and its divergence, which appear in the gas and solid governing equations.

$$\left(\vec{\Omega}.\nabla\right)I\left(\vec{r},\vec{\Omega}\right) = K(\vec{r})I_b(\vec{r}) - \beta(\vec{r})I\left(\vec{r},\vec{\Omega}\right) + \frac{\sigma_s(\vec{r})}{4\pi}\int_{\Omega'}\Phi\left(\vec{\Omega}',\vec{\Omega}\right)I\left(\vec{r},\vec{\Omega}'\right)d\vec{\Omega}' \tag{18}$$

where

$\vec{\Omega}$ = Solid angle
I = intensity of gas radiation, I_b = blackbody intensity at local temperature
K = absorption coefficient of the gas mixture, β = extinction coefficient
σ_s = scattering coefficient, Φ = scattering phase function

The local Plank-mean absorption coefficient for the gas mixture can be given as $P_{CO_2}k_{CO_2} + P_{H_2O}k_{H_2O}$, where P_i represents the partial pressure of species i. The values of k for each species were obtained from [27] as a function of temperature. The mean absorption coefficient is calibrated by following the work of [28]. The calibration is necessary because even for a flame as thin as one or two centimetres, the flame is not optically thin because of the self-absorption of the gaseous species in their radiating bands. It was shown that the Planck-mean results over-predict net emission from the flame. To improve the computed heat flux at the fuel surface or to the ambient surrounding, the absorption coefficient is calibrated against the narrow-band resulting through a quasi-one-dimensional flame which accounts for different optical lengths in different parts of the flame and the effect of spectral self-absorption of gaseous species. Therefore, the local absorption coefficient K used in this work is set to equal to CK_P, where C is the correction factor. In the downstream flame region of $X > 0$, C is determined by an optical traverse in the R-direction (perpendicular to the solid) and using the empirical relation proposed in [29]. For the region of $X < 0$ where the flame is highly two-dimensional, two traverses are made from $X = 0$, one in the Y-direction and the other in the upstream X-direction. The correction factor in this region is then the average of these two traverse values. A uniform C is assumed in this domain. Note that since the steady-flame solution is obtained iteratively, the distribution of C is also determined iteratively.

The boundary condition at the wall can be expressed as

$$I\left(r_w,\vec{\Omega}\right) = \varepsilon(r_w)I_b(r_w) + \frac{1-\alpha}{\pi}\int_{n\Omega'<0}\left|n.\Omega'\right|I\left(r_w,\Omega'\right)d\Omega'\ n.\Omega' > 0 \tag{19}$$

here, ε and α are the emissivity and absorptivity of the solid fuel.

The above set of governing equations and boundary conditions completely define the problem and can be solved numerically.

The Radiative Transfer Equation (RTE) can be represented using the Discrete Ordinate Method (DOM) as follows:

$$\xi\frac{\partial I\left(\vec{r},x,\vec{\Omega}\right)}{\partial x} + \frac{\mu}{r}\frac{\partial I\left(\vec{r},x,\vec{\Omega}\right)}{\partial r} - \frac{1}{r}\frac{\partial\left[\eta I\left(\vec{r},x,\vec{\Omega}\right)\right]}{\partial\psi} + \beta I\left(\vec{r},x,\vec{\Omega}\right) = S\left(\vec{r},x,\vec{\Omega}\right) \tag{20}$$

where

ξ, μ, η are the direction cosines in x, r and θ directions

Source term, $S(\vec{r},x,\vec{\Omega}) = k(\vec{r})I_b(\vec{r}) + (\sigma_s(\vec{r})/4\pi)\int_{\Omega'}\Phi(\vec{\Omega}',\vec{\Omega})I(\vec{r},\vec{\Omega}')d\vec{\Omega}'$

The RTE equation shown above can be written as a set of equations for each direction as follows:

$$\xi^{pq}\frac{\partial I^{pq}}{\partial x} + \frac{\mu^{pq}}{r}\frac{\partial(rI^{pq})}{\partial r} - \frac{1}{r}\frac{\partial}{\partial\psi}(\eta^{pq}I^{pq}) + \beta I^{pq} = S^{pq} \tag{21}$$

The index p indicates the value of ξ associated with the direction $\vec{\Omega}$ and the second index, q, increases with the value of μ associated with ξ.

The total incident radiation, radiative flux and the divergence of radiative flux can be calculated from the radiation intensity from the following formulae:

Incident radiation:

$$G(r,x) = \int_{4\pi} I\left(\vec{r},x,\vec{\Omega}\right)d\vec{\Omega} \tag{22}$$

Radiation heat flux in x and r directions:

$$q_r^{x+}(r,x) = \int_{\xi>0}\xi I\left(\vec{r},x,\vec{\Omega}\right)d\vec{\Omega} \tag{23.1}$$

$$q_r^{x-}(r,x) = \int_{\xi<0}\xi I\left(\vec{r},x,\vec{\Omega}\right)d\vec{\Omega} \tag{23.2}$$

$$q_r^{r+}(r,x) = \int_{\mu>0}\mu I\left(\vec{r},x,\vec{\Omega}\right)d\vec{\Omega} \tag{23.3}$$

$$q_r^{r-}(r,x) = \int_{\mu<0}\mu I\left(\vec{r},x,\vec{\Omega}\right)d\vec{\Omega} \tag{23.4}$$

The net radiation heat flux in x and r directions:

$$q_r^{x}(r,x) = q_r^{x-}(r,x) + q_r^{x+}(r,x) \tag{24.1}$$

$$q_r^{r}(r,x) = q_r^{r-}(r,x) + q_r^{r+}(r,x) \tag{24.2}$$

The divergence of radiative flux for the assumptions of emitting, absorbing and non-scattering gray medium is shown below:

$$\nabla.\vec{q}_r = k(r,x)\left[4\sigma T^4(r,x) - G(r,x)\right] \tag{25}$$

8. The solution procedure

The system of coupled elliptic partial differential equations for the flow and combustion in the gas phase is solved numerically by the SIMPLER/PISO algorithm [30]. The non-linear gas-phase equations are discretized using a finite-volume based difference technique. The velocities are stored at staggered grid locations with respect to scalar variables. The resulting set of algebraic equations are solved by sweeping plane-by-plane in each direction. Along each plane, a line-by-line procedure is used, which is a combination of Gauss-Seidel and the tridiagonal matrix algorithm (TDMA). In addition, the gas-phase system is coupled to the solid-phase equations, which are solved by the finite-difference technique. The steady flame spread rate (the eigenvalue of the whole system) is determined iteratively by using a bisection method to force the pyrolysis front (95% of the fresh fuel mass) to occur at $X = 0$. The Discrete Ordinate Method (DOM) is used for solving the RTE by sweeping in four directions as follows:

Sweep 1. $\xi^{pq} < 0$ and $\mu^{pq} < 0$ Sweep 2. $\xi^{pq} > 0$ and $\mu^{pq} < 0$
Sweep 3. $\xi^{pq} < 0$ and $\mu^{pq} > 0$ Sweep 4. $\xi^{pq} > 0$ and $\mu^{pq} > 0$

Since the radiation equation and the rest of the combustion/fluid equations are coupled, they are solved iteratively. In the present work, the radiation routine was invoked every 10 gas-solid

Table 1
Flame spread rates for different grid sizes in axial (x) and radial (r) directions.

Total number of grids in x and r-direction	Minimum grid size in x-direction (x $\bar{L}_R$)	Minimum grid size in r-direction (x $\bar{L}_R$)	Flame spread velocity (mm/s)
188 × 141	0.5	0.05	2.6
202 × 153	0.2	0.02	2.9
214 × 159	0.1	0.01	3.12
225 × 166	0.05	0.005	3.125
251 × 183	0.01	0.001	3.126

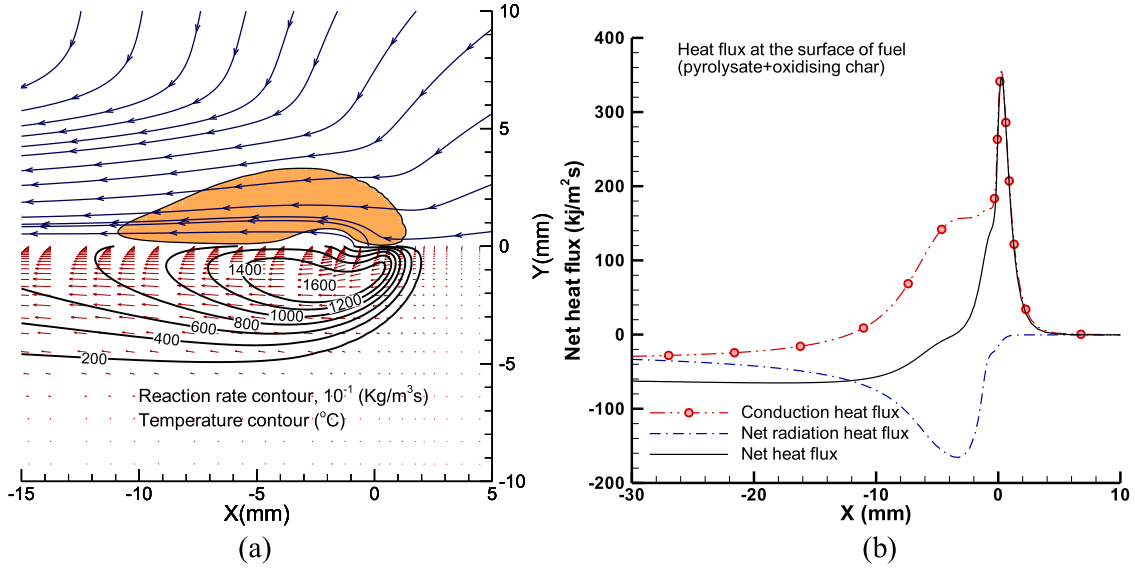

Fig. 4. (a) Computed flame structure of downward spreading flame over a pine needle, (b) heat flux distribution over surface of pine needle along its length.

iterations. Convergence to a steady state solution is determined by the fixed flame spread rate over a couple of thousand iterations in conjunction with satisfaction of continuity to the order less than 10^{-3}. Ideally it takes around 60,000 to 80,000 iterations to get convergence. The flame spread rates for different grid sizes in the x and r-direction are shown in Table 1. A grid size of 214 × 159 is chosen since more refinement of the grid has negligible effect on flame spread rate.

9. Results and discussion

The effect of char formation on downward flame spread rate over thin solid fuels, the prediction capability of the present model and its comparison with experiments, and the char oxidation phenomena are discussed in this section.

9.1. Influence of char on flame spread rate over thin fuel

A pine needle is a charring fuel; therefore, accounting for char formation is essential to modelling of flame spread over it. The present solid-fuel model accounts for char formation and its subsequent oxidation as indicated in Eqs. (17.1) to (17.3). Figure 4a shows the detailed flame structure of downward spreading flame in flame-fixed coordinates predicted by the present quasi-steady flame spread model with all input data from [31] and for no external flow. The upper half of the figure shows streamlines and the flame shape represented by the area enclosed within the reaction rate contour of 10^{-4} g/cm^3/s. Stream-lines originating from the fuel surface show fuel pyrolysate emerging from the fuel surface. The streamlines also show entrainment of surrounding air towards the flame. Considering symmetry about the fuel surface, the flame is tear shaped about 1 cm long and 0.6 cm wide. The lower half of the figure illustrates temperature contours in the flame and the flow field vectors. The velocity vectors show flow accelerates in the hot buoyant plume downstream of flame. The maximum flame temperature reaches a little above 1600 °C. The flame leading edge is located at about X = 0 where the flame anchors on the fuel surface. Figure 4b shows the computed heat flux distribution along the pine needle surface. The figure shows conductive-convective heat flux (mentioned here as conduction heat flux) and net radiation heat flux components (the sum of flame radiation feedback and surface radiation loss) along with total or net heat flux. It is clear that conduction is the only significant source of heat feedback from flame to the fuel surface and net radiation heat flux is the heat loss component. This indicates that the flame radiation feedback from flame to fuel surface is negligible as compared to conduction heat flux. However, flame radiation is important to account for the radiation heat loss from the flame to obtain a correct flame temperature prediction. Here flame radiation loss was found to reduce flame temperature by about 200 °C. The heat flux distribution shows an intense heat flux (with peak reaching in excess of 350 kW/m^2) just downstream of the flame leading edge that steeply decays away from the peak location over a span of 2-3 mm. In the region x < −10 mm conductive heat flux at the fuel surface is negative, this is because of the fact that the surface temperature is higher than the gas temperature owing to the exothermic char oxidation reaction. The computed flame spread rate for the above case was found to be 3.2 mm/s.

In the presence of char in the fuel, the flame spread rate decreases with increased char amount [7]. For thin fuels, the decrease in the flame spread rate could be due to several factors. To assess the role of these factors, char formation was modelled in two ways. In the first model (Eq. (17.4)), char is treated as inert mass which is left over after all the pyrolysate is gone. In this model, as long as pyrolysate is present, char is considered to be not

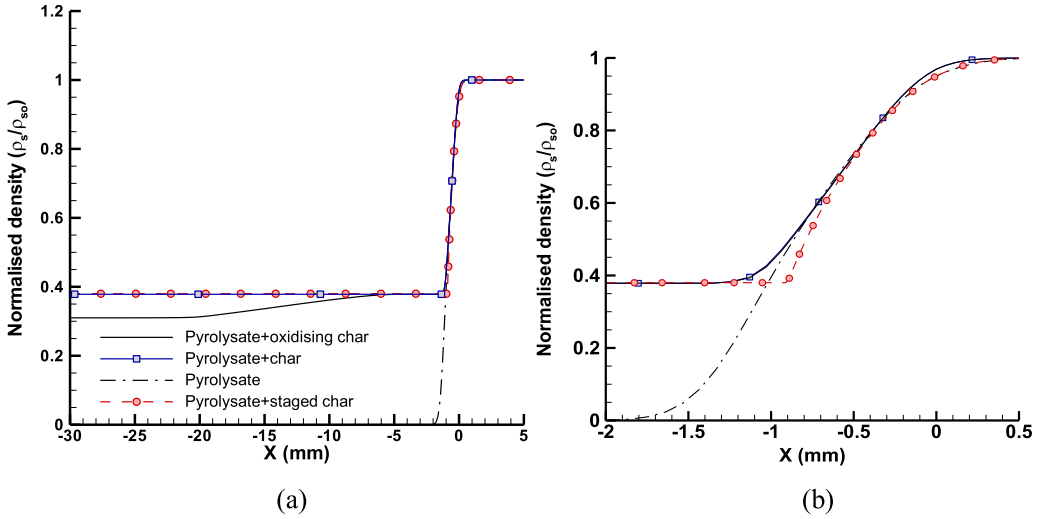

Fig. 5. (a) Effect of pyrolysis model and char oxidation on normalised fuel density along the fuel length. (b) close up of the pyrolysis region shown in (a).

exposed. This model is similar to the fuel model of composite fuels, such as cotton fabric woven over fibre glass [32]. Here we refer to this model as a 'staged char model'. In the second model, referred here as a 'simultaneous char model', pyrolysis of virgin fuel results in simultaneous formation of pyrolysate vapours and char. This later model provides a more realistic description of char formation and has therefore been used by researchers [3–8]. In addition to above char models, two additional simulations were made. In case one, fuel was assumed to consist of pyrolysate alone (i.e. no char present, Eq. (17.4)) and in the second case, the char formed by the simultaneous char model is assumed not to oxidise (Eq. (17.1) where $\dot{m}_C'''$ is zero).

The flame spread rate computed for the 'no char' fuel comprising entirely of pyrolysate was found to be 6.6 mm/s. The computed flame spread rate for the case of 'staged char' model was found to be slightly lower at 6.2 mm/s, which in turn is about two times higher than the computed flame spread rate of 3.2 mm/s for both 'simultaneous char' models (i.e. with and without char oxidation). Nearly the same spread rate in cases of char oxidation and no char oxidation indicates there is negligible influence of char oxidation on the flame spread rate.

One effect of char is to act as a heat sink in the fuel preheat region by absorbing a part of the heat feedback from the flame and thereby not contributing to the heat release in the flame. It is interesting to note that the flame spread rate decreases by only about 6%, when the flame spread over no-char fuel is compared with the flame spread over charring fuel (staged char model) with nearly 38% char. It is even more interesting to note that the flame spread rate substantially differs between the two char models (nearly 50% drop with respect to the 'staged char' model). Figure 5 shows variation of pine needle density normalized to virgin pine needle density with distance along the pine needle. The curves shown in the figure correspond to different char fuel models, namely, the 'staged char' model, 'simultaneous char model' and 'oxidising char'. In Fig. 5, downstream of the flame anchor location (X = 0) the pine needle density drops steeply over a distance of just about 1 mm seemingly identically for all the three fuel models. The drop in density corresponds to pyrolysate present in the virgin fuel. For the oxidising char model, the fuel density further decreases gradually about 4–5 mm downstream of the pyrolysis region before remaining constant beyond some distance (here 30 mm). However, this constant density is significantly higher than the density where only ash is left (3.8%). This implies that beyond some distance char does not oxidise anymore. Figure 5 shows a close-up of the pyrolysis region. While the difference due to three fuel models can be seen more clearly here, the curves are still close, especially those for the 'simultaneous char' and 'char oxidation' models. At any location on the pyrolysing needle, the normalised density is lower for the 'staged char' model, compared to the 'simultaneous char' model.

The two char production models differ in pyrolysate mass flux distribution along the fuel surface. The fuel mass flux corresponding to the two char formation models is shown in Fig. 6a. Also shown in the figure is the pyrolysate mass flux in the case where no char is present in the fuel. The pyrolysate production for the 'staged char' model (and also no-char case) starts further upstream and has significantly higher mass flux for most locations on the pine needle surface, compared to pyrolysate production by the 'simultaneous char' production model. Since the flame spread rate is directly proportional to heat feedback from the flame to the pine fuel upstream of the flame front, higher fuel mass flux near the leading edge would result in higher conduction heat feedback to the fuel in the preheat region ahead of flame.

Figure 6b compares net heat flux profiles for the two char production models. The net heat flux profiles clearly show higher heat flux for 'staged char' model (and also for no char case) in the preheat region which extends further upstream compared to the 'simultaneous char' model. The flame shapes represented by the enclosed area of reaction rate contour 10^{-4} g/cm^3/s and the temperature field of the spreading flames for the two char models are shown in Fig. 7a and b. Clearly the flame front for the 'staged char' model is further upstream of X = 0 (determined by location of 5% reduction in fuel density) of the flame front for the 'simultaneous char' model. Due to higher fuel mass flux, the flame is longer and hotter, as well, for the 'staged char' model. The phenomenon of char oxidation does not affect pyrolysate mass flux distribution at the fuel surface and heat flux distribution in the preheat region and hence the flame spread rate. However, the difference between the case of 'char oxidation' and the case of 'no char oxidation' can be seen in the surface temperature (Fig. 8a and b). Figure 8a and b show the fuel temperature along the pine needle and temperature in the flame at a distance of 1 mm above the fuel surface for the case of 'no char oxidation' and the case of 'char oxidation', respectively. The surface temperature is always lower than the gas temperature when char does not oxidise but when char oxidation is considered, the fuel temperature is seen to increase

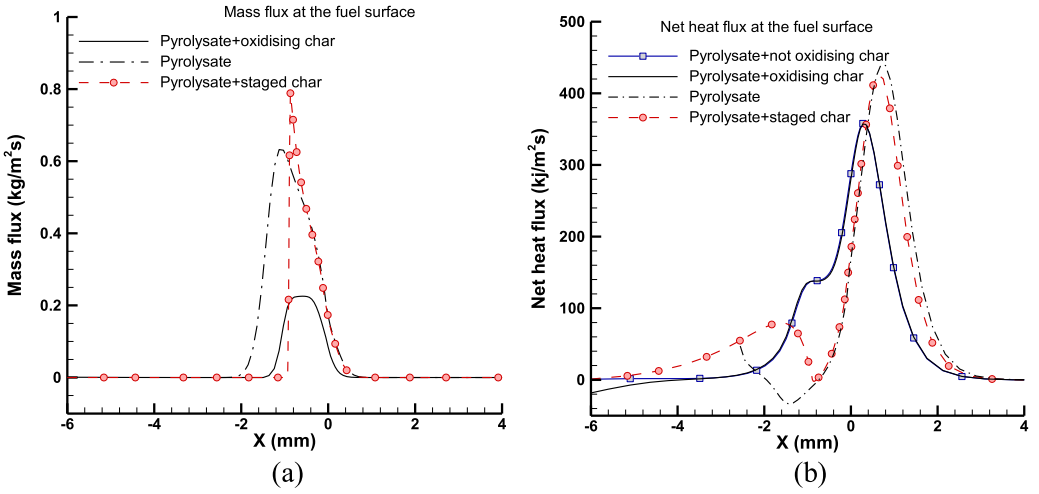

Fig. 6. (a) Fuel vapor mass flux distribution at the fuel surface and (b) net heat flux distribution on the fuel surface, for two pyrolysis models.

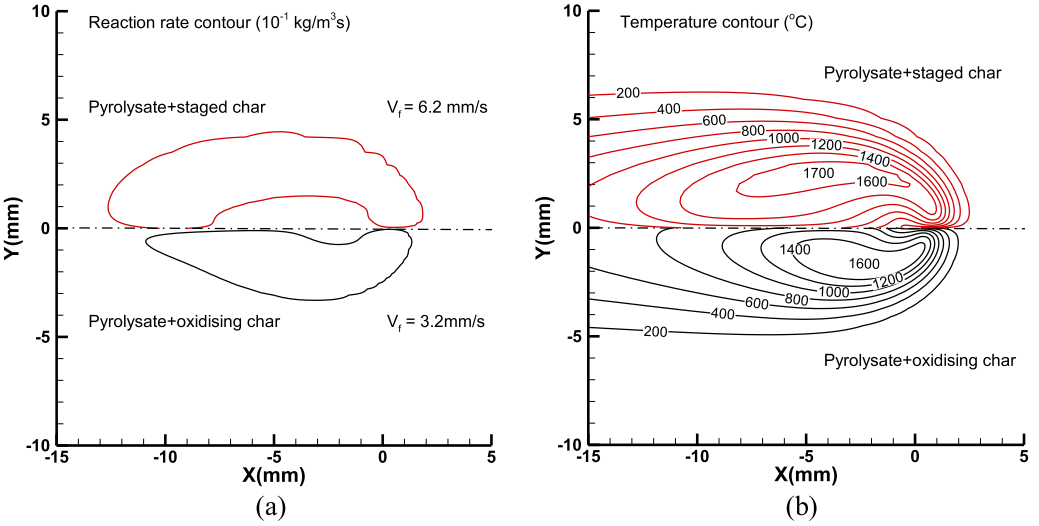

Fig. 7. Flame structure illustrated by (a) region enclosed by reaction rate contour of value 10^{-1} kg/m^{3}s and (b) spatial temperature distribution in gas phase for two pyorlsyis models.

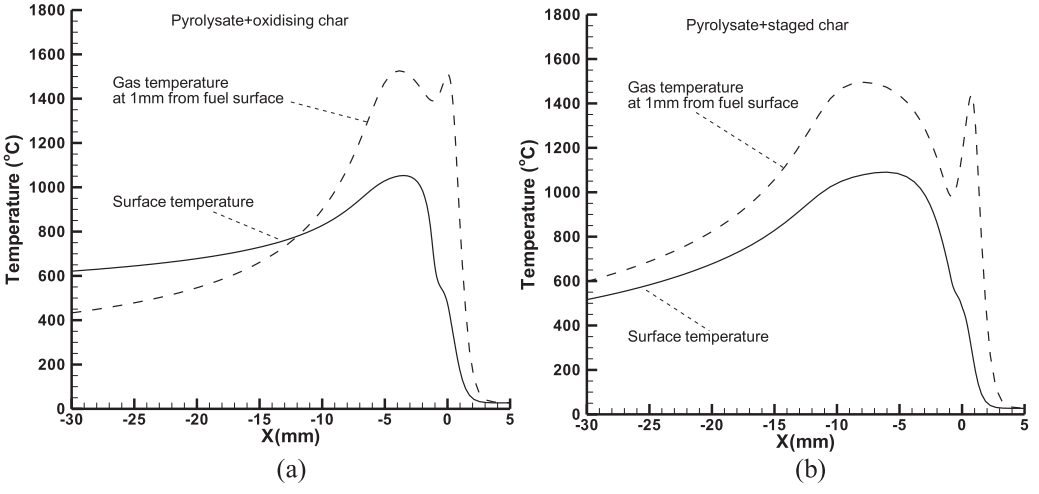

Fig. 8. Variation of surface temperature and flame temperature (at 1 mm from surface) along the length of pine needle for two pyrolysis models (a) pyrolysate + oxidising char, (b) pyrolysate + staged char.

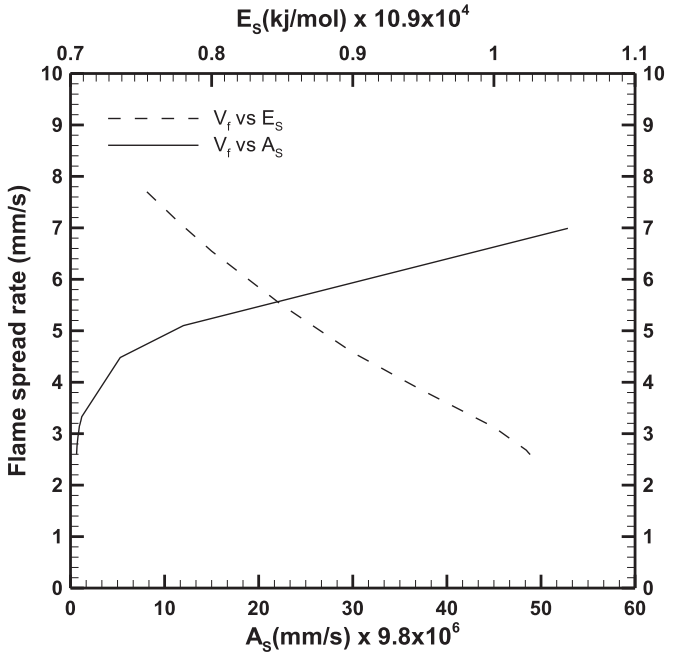

Fig. 9. Variation of flame spread rate with pyrolysis law constants E_s and A_s.

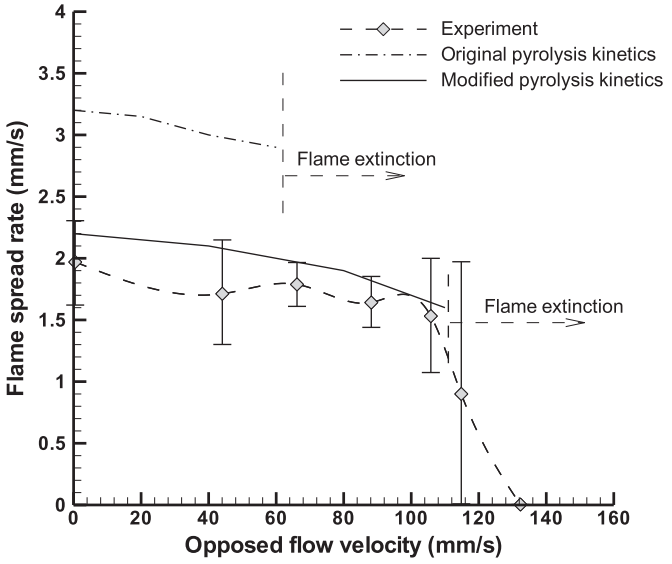

Fig. 10. Variation of downward flame spread rate over a single pine needle with opposed flow velocity.

significantly higher than the neighbouring gas temperature owing to heat release from oxidation of char.

9.2. Comparison of numerical prediction of the downward spreading flame over a single pine needle with experiments

The present model has evolved from an existing numerical model [25] with extensive modification to predict details of downward spreading flame and over thin cylindrical cellulosic charring solid material. As mentioned before in this collaborative research work, detailed measurements on downward spreading flame over a single pine needle [19] has been carried out to provide data for model validation. In this study, detailed scalar field variables, like temperature and species concentration, have been measured along with the fuel temperature profile. The work also provides consistent fuel properties and reaction kinetic information. In the framework of all this information, the present numerical model is assessed for its prediction capability and validated. The information related to gas phase combustion reaction kinetics and to some extent the fuel pyrolysis kinetics need to be calibrated with the experimental data. The flame spread rate predicted using gas phase reaction combustion kinetics from [33] for ethanol combustion and pyrolysis kinetics is taken from [31], as mentioned earlier in the context of Fig. 4. The deviation from the pyrolysis kinetic data of [19] is expected as the data were obtained using TGA at the heating rates which were much lower, compared to what is observed in the pine needle flame spread experiments. The computed flame spread rate for this case is 3.2 mm/s, which is about 60% higher than the corresponding experimental value, 2 mm/s.

A parametric study was carried out to investigate the influence of pyrolysis kinetic parameters on the flame spread rate. Figure 9 shows variation of the flame spread rate with the pre-exponential factor (As) and the activation energy (Es) in pyrolysis kinetics. The flame spread rate can be decreased if Es is increased or As is decreased. It is also to be noted that beyond certain values of Es and As the flame extinguishes. Since rapid pyrolysation processes are known to have low values of Es, As was decreased and in order to assure the flame not prematurely extinguish, the pre-exponential factor (Bg) of gas phase combustion reaction was increased. This trial and error process was continued with one more constraint on flame extinction. Experiments in [19] were carried out under various opposed flow conditions where the external opposed flow velocity was varied from no flow (0 mm/s) to about 130 mm/s until the flame consistently failed to spread down the vertical pine needle. Therefore, the value of As and Bg were calibrated such that the flame spread rate was within the error bar of 2 mm/s experimental spread rate and the extinction opposed flow velocity is between 11 cm/s and 12 cm/s as observed in experiments. Figure 10 shows the variation in the measured flame spread rate with externally imposed opposed flow velocity. Also shown in the figure are the predicted flame spread rates using kinetic parameters modified by the process explained above and original parameters used in the numerical prediction in Fig. 4.

In Fig. 4 structure of downward spreading flame over a single pine needle was shown. In this case there was no externally opposed flow. However, in presence of an external opposed flow, the flow field is expected to be quite different with presence of velocity gradient due to boundary layer over the pine needle. Figure 11 shows flame at no external flow (Fig. 11(a)) and spreading flame for imposed external flow of 8 cm/s (Fig. 11(b)). The flame is represented by contour of reaction rate 10^{-4} g/cm^{3}s and flow field represented by streamlines and velocity vectors in flame fixed reference at about 5 mm upstream and downstream of the flame leading edge. One can note that for the pure downward spread (Fig. 11(a)) air is drawn from the sides, the small amount of air from upstream is due to flame spread velocity which is seen as inflow from upstream in flame fixed frame of reference. In the presence of externally imposed opposed flow most of the flow to the flame is seen (Fig. 11(b)) coming from upstream and the flame is situated within the boundary layer. The flame is smaller and closer to surface compared to the case of no external flow indicating increased convective heat loss from the flame which eventually leads to flame extinction by blow-off at about 12 cm/s.

As mentioned before, the flame spread rates predicted using original kinetic parameters are higher than corresponding experimental values and at the same time extinguishes at a much lower opposed-flow velocity (of about 6.5 cm/s), compared to those measured in experiments. The flame spread rate, which is an

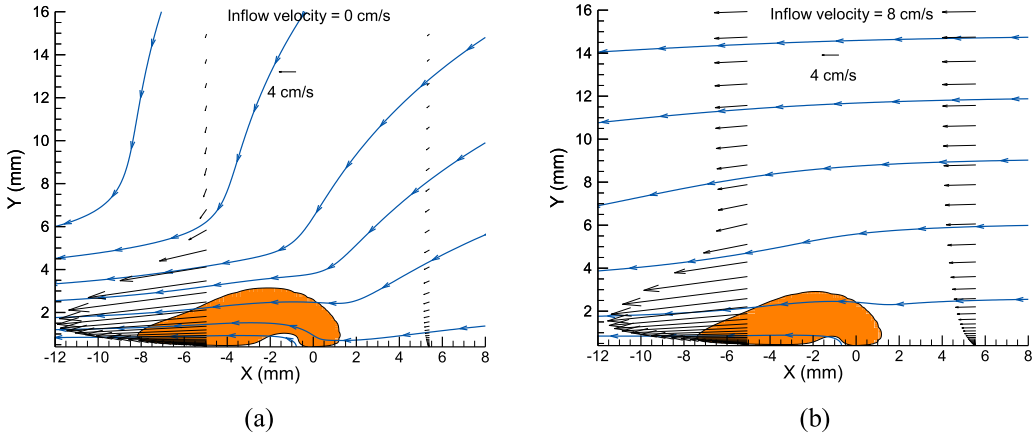

Fig. 11. Flame shape (area enclosed by reaction rate contour of 10^{-4} g/cm^{3}s) and velocity field (shown by streamlines and velocity vectors in flame fixed frame of reference, at about 5 mm upstream and downstream of flame leading edge) for downward spreading flame over a pine needle subjected to opposed inflow velocity of (a) 0 cm/s, (b) 8 cm/s. The gravity vector is directed to the right.

eigenvalue in the solution of the present numerical model and the flame extinction opposed velocity are two important global value parameters used for calibrating the kinetics parameter for combustion and pyrolysis. Adoption of modified kinetic parameters thus obtained resulted in better prediction of the flame spread rates with opposed velocity. However, these global values depend on non-linearly coupled complex flow, heat and mass transport processes that take place in the flame spread process. In order to ensure consistency of the numerical model in predicting actual physical processes adequately, it is vital to examine the numerical prediction with more detailed measurements in the spreading flame. In the preceding work [19], a detailed flame structure measurement involving spatial measurement of temperature and species was carried out. Therefore, detailed scalar fields of temperature and species obtained numerically for the case of downward spreading flame over a single pine needle with no externally opposed flow is compared with corresponding data from experiments. Before we look at these comparisons, it is useful to review how data is measured and what numerical data from a simulation represents. It was mentioned earlier in the section describing experiments that the measuring probe (a thermocouple or pneumatic probe) in the gas phase was located at about the mid of the length of the pine needle and at a distance perpendicular to the needle surface, which varied from 0.2 mm (1 mm for concentrations) to 7 mm. For each experiment, the position of the measuring probe was kept at a fixed distance from the surface and the scalar data (temperature or concentration) was recorded with time. This scalar-time data was translated to scalar-space data by using the measured steady flame spread rate. The complete temperature field was obtained after several experimental runs with the measuring probe placed at a different perpendicular location above the fuel surface. The experiment has transient segments, namely, the ignition to steady state transition (see Fig. A2(a) of the Appendix or Fig. 7(a) of [19]) and steady state to end of burn (see Fig. A2(d–g) of the appendix or Fig. 7(d–g) of [19]) when the spreading flame reaches the bottom end of the fuel. The former can be eliminated by starting the count of time when steady state is attained, the latter one requires longer specimens which were difficult to handle for two reasons; one, it is difficult for a pine needle to be straight and two, it is difficult to insert a thermocouple in it for fuel temperature measurement. On the other hand, the numerical model solves for the quasi-steady flame located at about the centre of the pine needle of finite length to account for the end effect. However, in the experiments temperatures are measured at the middle of the pine needle (at about 12.5 mm from one end) with time. This local temperature versus time data is translated into temperature versus distance plot by making use of measured steady spread rate. When using this approach to describe spatial temperature variation along the pine needle, a steeper drop in temperature downstream of flame is obtained corresponding to the flame positions very close to the lower end on the pine needle to the point it quenches. If the pine needles used in experiments were longer it would be possible to get much closer match of temperature and species profiles between simulations and experiments for downstream segment beyond – 5 mm. This was however, not possible because pine needle length limitation was posed by the want of straight segment of pine needle for experiments and challenge in inserting thermocouple inside the pine needle along its length. Other approach would be to have a more complex and involved complete transient simulation (not in flame fixed co-ordinates) of the flame spread process. Therefore, deviations between experiments and numerical prediction are expected further downstream of the spreading flame. However, this segment which is far downstream has practically no influence on flame spread process.

Figures 12–19 present comparisons of scalar data measured in experiments and corresponding numerical prediction. These are discussed next in order. Figure 12 shows the complete temperature field for a downward spreading flame over a single pine needle. In the figure, the flame is spreading from left to right with the gravity vector pointing to the right.

The upper half of the figure shows temperature contours from experiments and the lower half shows the corresponding contours obtained from the simulation data. The experimental flame width is about 6 mm and that in the numerical simulation is nearly same at about 5 mm. The maximum flame temperatures are of the same order - about 1600 °C. A more detailed comparison of flame temperature distribution is shown in Figs. 13 and 14. Figure 13 shows the temperature profile along the length of a pine needle at locations 0.2 mm, 1 mm, 2 mm, and 3 mm above the surface of the pine needle, and Fig. 14 shows temperature profiles in the direction perpendicular to the pine needle surface at locations of 8.2 mm and 12 mm downstream of the flame leading edge. The experimental temperature measurements shown are measured by two different approaches, namely, thermocouple and micro probe [19]. Figure 13a–c show very good qualitative and quantitative match of experimental and predicted temperature profiles. The difference between the experiment and simulation is noted further downstream of the flame leading edge (between $X < -5$ to -10 mm), which as

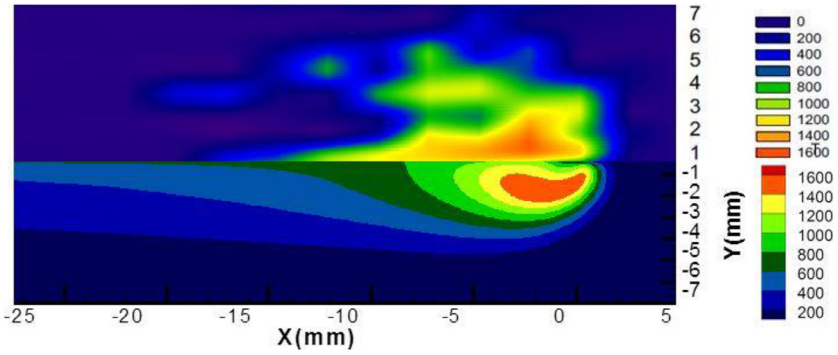

Fig. 12. Comparison of measured flame temperature (upper half) and predicted flame temperature (lower half).

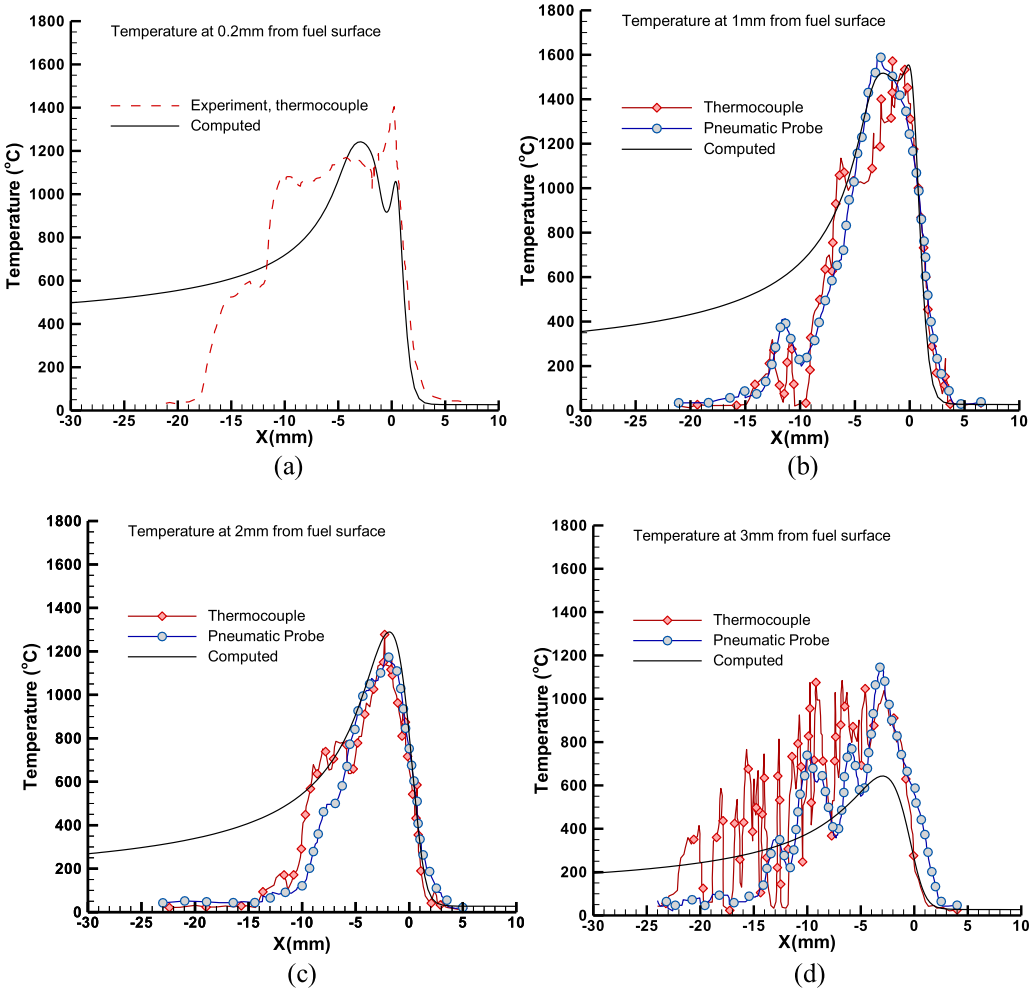

Fig. 13. Comparison of measured (thermocouple and pneumatic probe) and predicted flame temperature in the direction along the pine needle at a distance of (a) 0.2 mm and (b) 1 mm, (c) 2 mm and (d) 3 mm from the pine needle surface.

explained before is due to transient processes towards the end of burn where the flame stops and goes out.

Due to this, the quasi-steady flame spread prediction shows slower decay in flame temperature further downstream compared to experiments. The experimental temperature profile for $Y \geq 3$ mm shows large fluctuations in measured temperature (as in Fig. 13d for $Y = 3$ mm) for both thermocouple and micro probe measurements. These fluctuations in measured temperature are caused by flame fluctuations, related to variations in the evolving of pyrolysis products (gas micro jets) from the pine needle surface [19]. Therefore, comparison with simulation is not made for $Y > 3$ mm. The transverse temperature profiles shown in Fig. 14 also show good match of the experiment and the predicted temperature data. However, further downstream (at location 12 mm, Fig. 14b), the difference between the experiment and the simulation data is again due to transient processes at the end of needle.

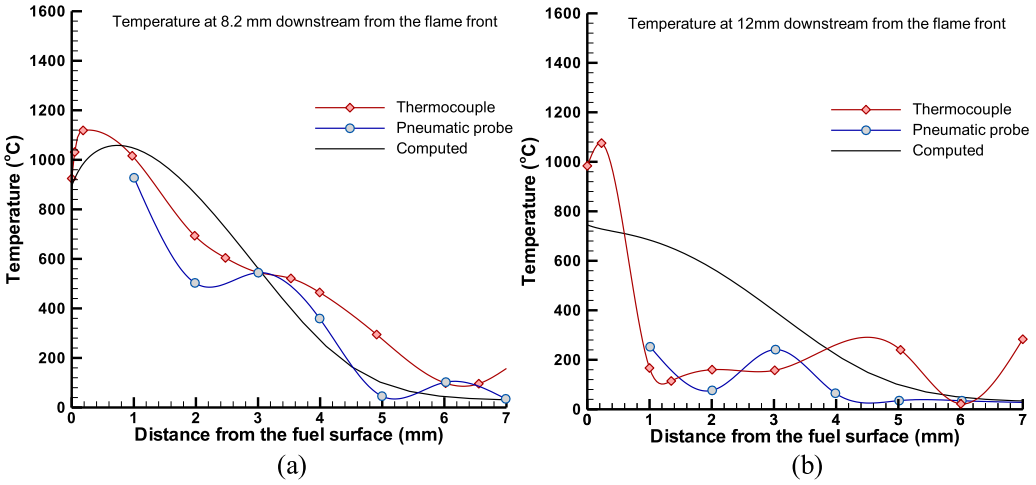

Fig. 14. Measured and predicted flame temperatures perpendicular to the pine needle at a distance of (a) 8.2 mm and (b) 12 mm downstream from the flame front.

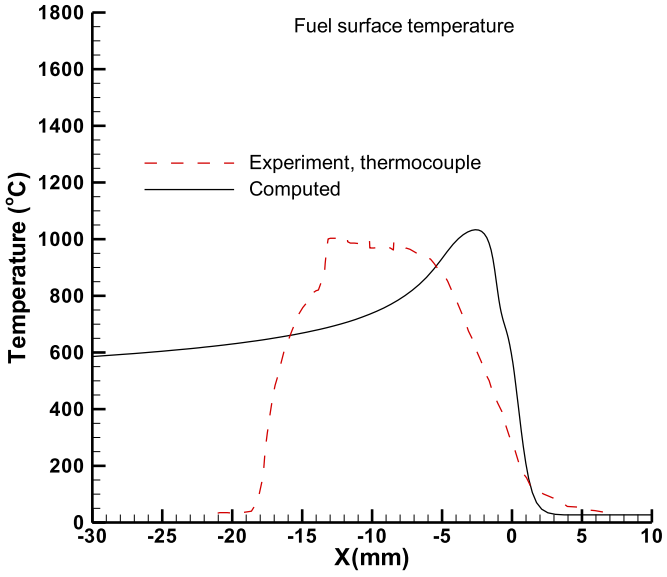

Fig. 15. Measured and predicted surface temperatures along the pine needle.

Figure 15 shows the measured and predicted fuel temperature along the pine needle. Except for the difference due to end of burning further downstream, the two curves are qualitatively the same and the peak temperatures nearly the same. However, the predicted temperature profile shows a steeper rise in temperature compared to the experimentally measured profile. The thermocouple was placed centrally along the length of the needle; therefore, this difference may be due to the 'thermally thin' approximation made in the model. Subsequently the temperature difference between the surface and the centre of the pine needle was also measured in another test and the two differed by about 70 K, indicating the existence of a thermal gradient inside the pine needle.

Figure 16 compares the measured and predicted CO2 concentration along the needle length at distances 1 mm and 2 mm from the pine needle surface. Figures 17 and 18 show similar comparison of water vapour and oxygen molar fractions, respectively. The figures illustrate a good match of measured and predicted trends. The CO_2 and H_2O are somewhat over-predicted, and consequently O_2 is under-predicted. It is interesting to note that there is almost no available oxygen close to the pine needle surface for some length immediately downstream of flame leading edge where there is a strong reaction zone. The fuel vapour and product gases in the flame shield the charring pine needle from getting exposed directly to the ambient oxygen. This is why char oxidation takes place after passage of the flame leading edge when surrounding oxygen can finally diffuse to the needle surface. Since the fuel samples were short (about 25 mm) the effect of end of burning shows up in experiments where the oxygen molar fraction steeply rises to near ambient values. On the other hand, the simulation results for quasi-steady flame spread show a more gradual rise in the oxygen level. Simulations for higher opposed flow velocities show a progressive reduction in length of low oxygen region with increased opposed velocity; consequently, char oxidation begins closer to the pyrolysis front.

The profiles of the molar fractions of O_2, CO_2 and H_2O (both measured and computed) are also plotted with distance perpendicular to the surface of the pine needle at locations about 2.3 mm and 3.5 mm downstream of the flame leading edge. Since concentration data using micro-probe was measured closest up to 1 mm from the pine needle surface, the measured and computed profiles are plotted for distances within the range from 1 mm to 7 mm from the fuel surface. The computed and measured profiles show a reasonably good match. These comparisons and those presented in earlier figures also suggest that over all flame structure has been well captured by the present numerical model.

9.3. The char oxidation phenomenon

The detailed species measurements revealed negligible oxygen levels for a few millimetres downstream of the flame leading edge. This suggests that the char oxidation process can become significant only at locations further downstream. This fact is also reflected in the results of the numerical simulations. For example, in Fig. 5a region with nearly constant normalized density just downstream of the location where pyrolysis ends indicates negligible char oxidation. The normalised density decreases due to char oxidation only further downstream and stops decreasing again at some point further downstream.

Near the end of burning when the flame reaches the bottom of the needle, the flame reduces in size and extinguishes. This result is sudden or steep increase in availability of oxygen at the surface of charred pine needle causing it to oxidize rapidly.

Due to this rapid char oxidation, the pine needle temperature is significantly higher in experiments for distances further down-

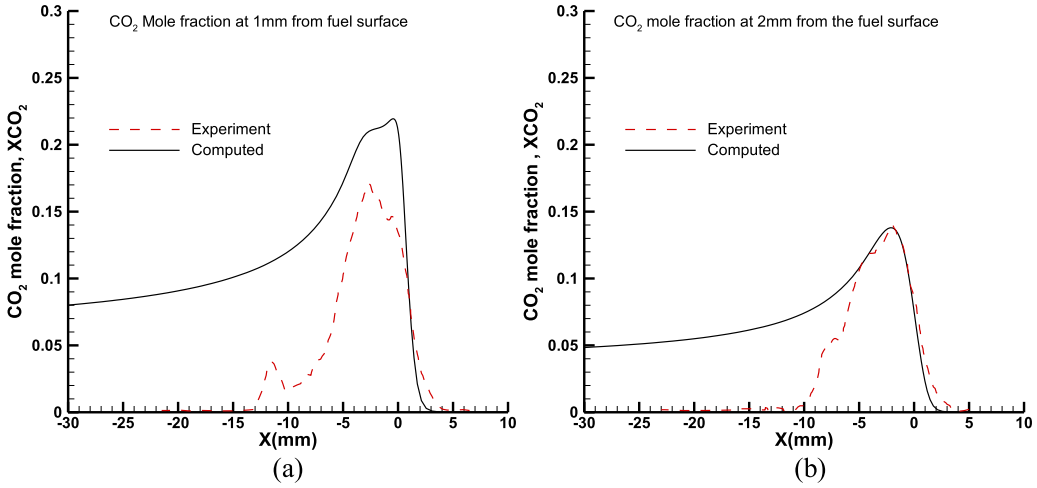

Fig. 16. Comparison of measured and computed carbon dioxide mole fractions along the pine needle at a distance of (a) 1 mm and (b) 2 mm from the pine needle surface.

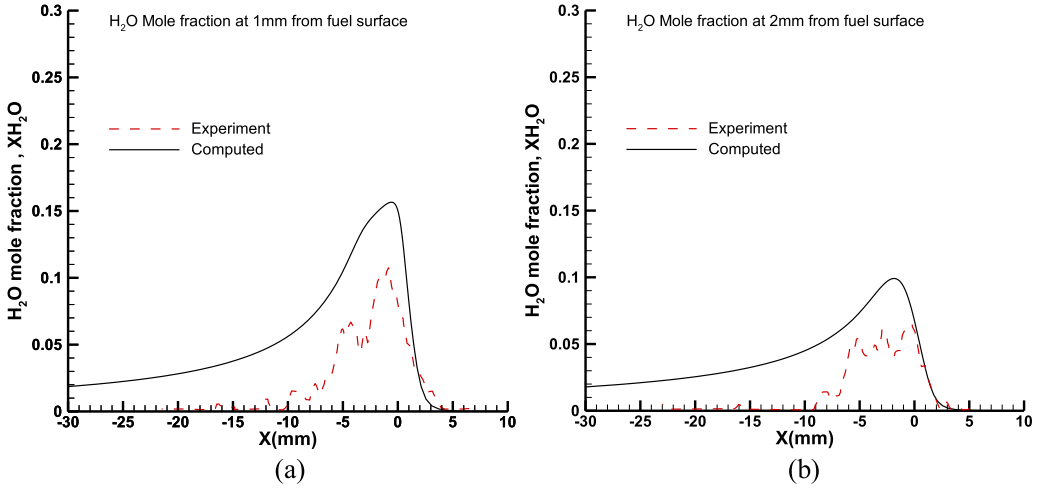

Fig. 17. Comparison of measured and computed water vapour mole fractions along the pine needle at a distance of (a) 1 mm and (b) 2 mm from the pine needle surface.

stream of about 8 mm (Fig. 15). On the contrary, in quasi-steady numerical predictions the rising plume of combustion products continue to shield the charred pine needle from direct exposure to atmospheric oxygen and so oxygen diffuses to the surface gradually over a distance and thus predicts low char oxidation rates compared to experiments and hence lower and gradually decreasing pine needle temperature. At some point where the temperature drops low enough, char oxidation is not significant any longer and in such a situation there is no further change in the pine needle density, as noted in Fig. 5.

Although there are differences in the present comparison of the rate of char oxidation due differences in the conduct of experimental and numerical conditions, it is nevertheless useful to understand the factors involved in the char oxidation process. The char oxidation phenomenon has been investigated in the past. Typically char oxidation rate depends on transport of oxygen to the hot char followed by its diffusion into the solid mass and subsequently its reaction with char. The rate of char oxidation is determined by the slowest of the three serial processes involved. In the case of a pine needle owing to its small thickness, only transport of oxygen from ambient air through the combustion product plume layer and reaction kinetics of char oxidation are considered as competing effects in determining the overall char oxidation rate. The slower of the two processes controls the overall char oxidation rate.

In order to study the contribution of char oxidation kinetics and diffusion, a set of simulations were carried out where the pre-exponential factor in the char oxidation kinetics was varied. Figure 20a shows variation of char density normalised to virgin fuel density along the length of a pine needle and Fig. 20b shows the corresponding pine needle temperature. For the original char kinetics (Fig. 5), one can note that first there is a steep increase in char density due to formation of char from the pyrolysis process, then char density remains constant at about 0.4 (which is carbon + ash fraction in the virgin fuel) for about 4 mm and, finally char density decreases as char oxidises to carbon dioxide and leaves behind ash. As noted in Fig 20a (and Fig. 5), at some point downstream (here when normalized char density is 0.26) char stops oxidizing any further. The pine needle temperature (Fig.20b) also falls more steeply, as there is no heat release in the pine needle due to char oxidation. The pre-exponential factor in char oxidation kinetics was increased by one order, two orders and four orders. The corresponding curves are identical except that char oxidation does not stop as in the case of original kinetic parameters and continues to decrease. Identical char density curves and pine needle temperature curves show that the char oxidation process is limited by oxygen diffusion to the surface and char oxidation kinetics control only in regions where there is surplus oxygen.

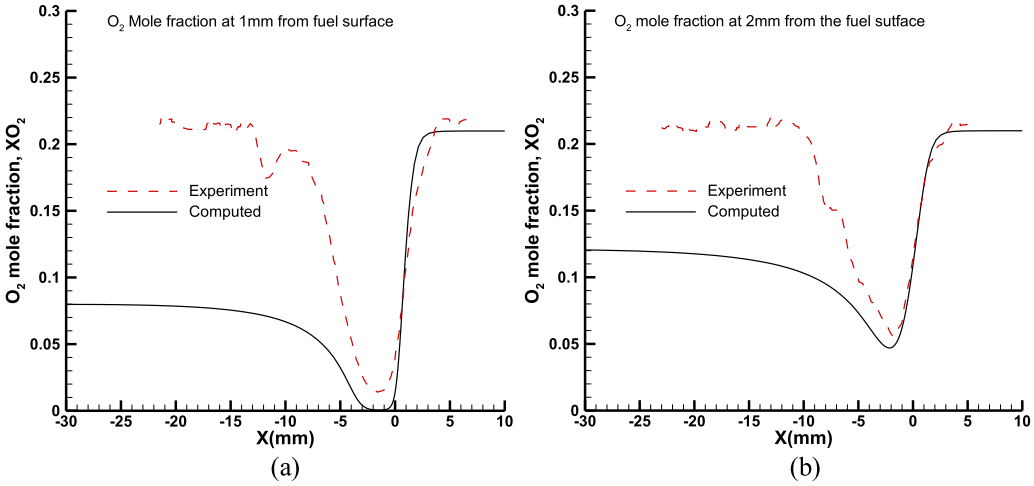

Fig. 18. Comparison of measured and computed oxygen mole fractions along the pine needle at a distance of (a) 1 mm and (b) 2 mm from the pine needle surface.

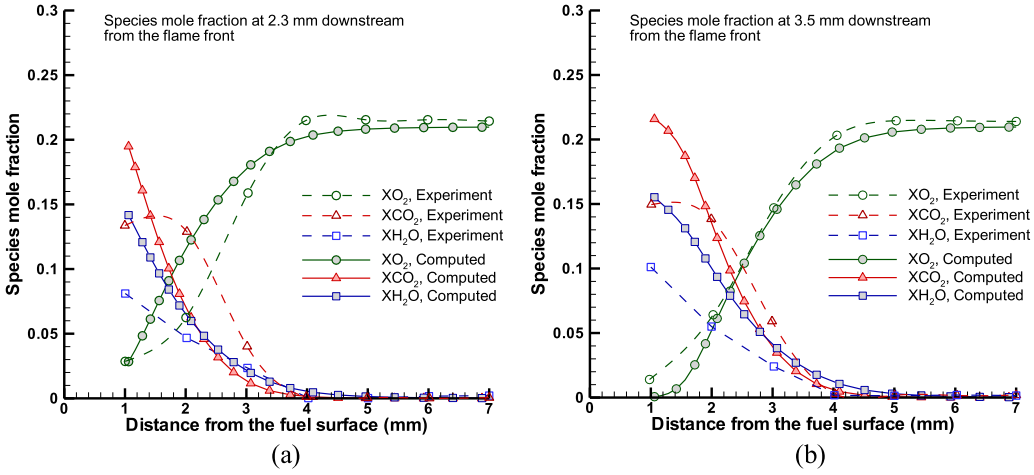

Fig. 19. Comparison of measured and computed specie mole fractions (CO_2, H_2O and O_2) perpendicular to the pine needle at a distance of (a) 2.5 mm and (b) 3.5 mm from the flame front.

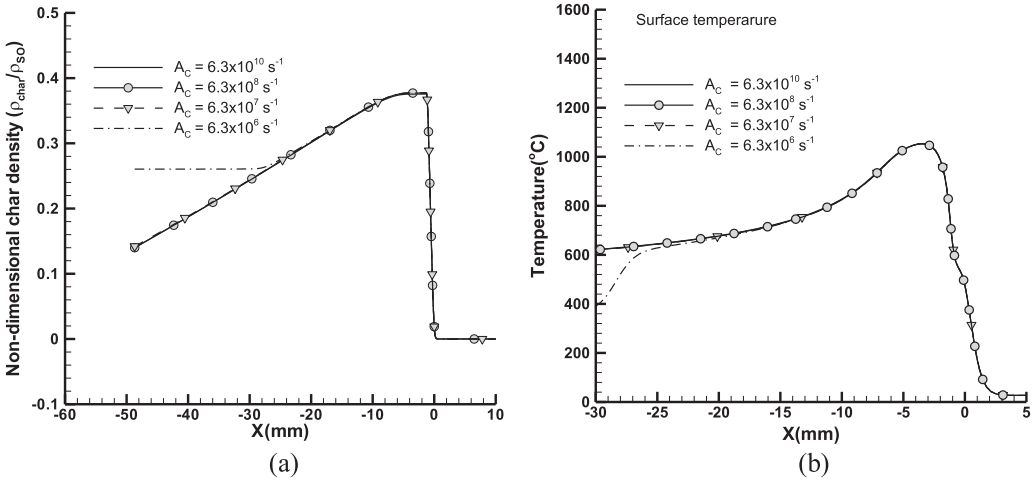

Fig. 20. Variation of (a) char density and (b) surface temperature with distance along pine needle for various char oxidation reaction rates.

To clearly identify the roles of char oxidation kinetics and oxygen diffusion, the oxygen mass flux required for oxidising available char by oxidation reaction is determined in addition to oxygen mass flux available by the convection diffusion process at the surface of the pine needle. The process with lower oxygen flux dictates the overall oxidation process. Figure 21 compares the oxygen mass flux for the two processes along the length of pine needle. It is interesting to note (see Fig. 21a and b) that the available oxygen mass flux by diffusion shows a sharp increase near the flame leading edge (about X = 0) and at some distance down-

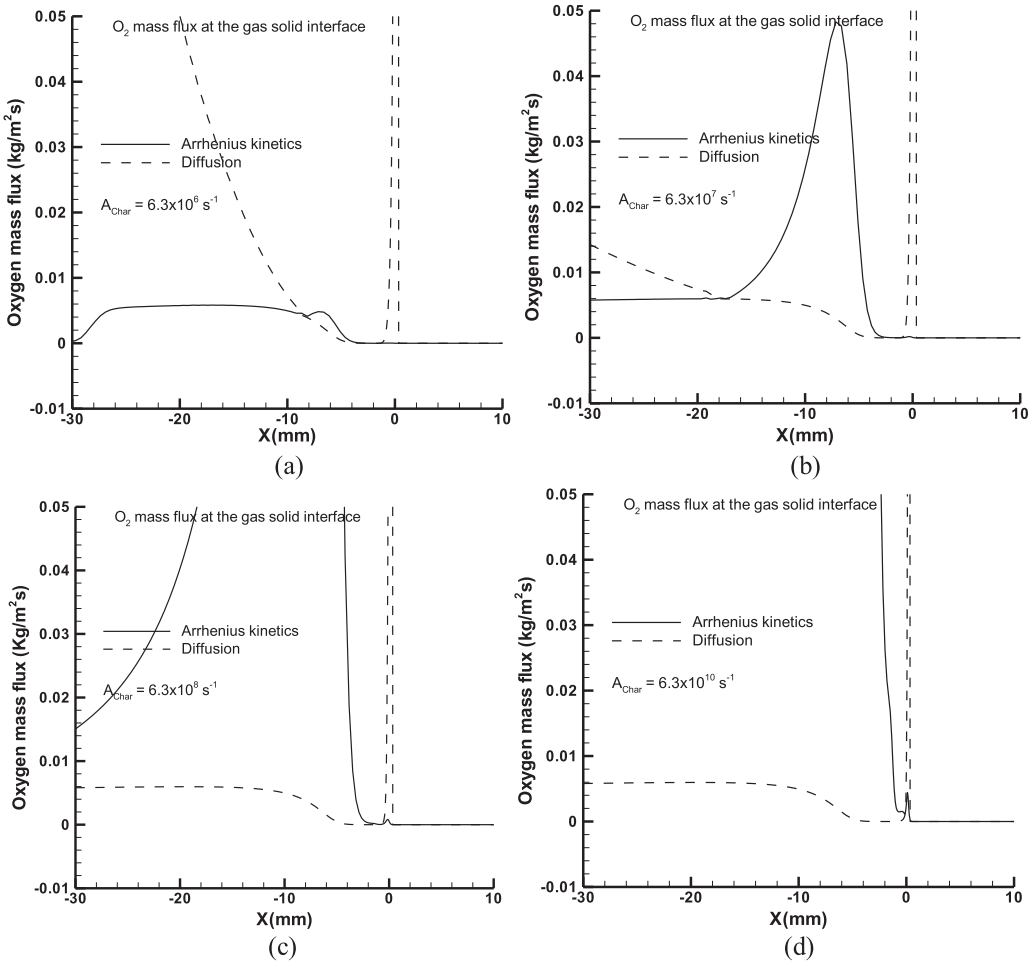

Fig. 21. Computed oxygen mass flux distributions at the pine needle surface due to kinetically controlled char oxidation and diffusion controlled char oxidation.

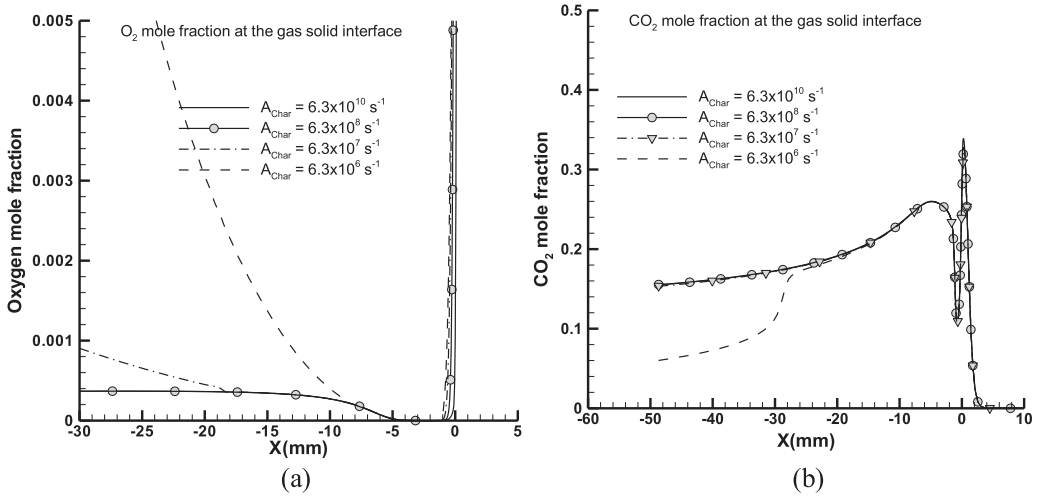

Fig. 22. Variation of (a) oxygen mole fraction and (b) carbon dioxide mole fraction with distance along pine needle at pine needle surface for various char oxidation reaction rates.

stream of the flame. This is due to high oxygen levels close to the pine needle surface in these regions (see Fig. 22a). In-between is the region of low oxygen diffusion mass flux due to fuel mass efflux at the surface and flame enveloping the pine needle surface which consumes oxygen diffusing from the ambient. The oxygen mass flux required for oxidising the available char exhibits a peak in the region, where available oxygen is at a minimum. The two oxygen mass flux curves are useful to describe the char oxidation process in the pine needle. In the preheat region as the pine needle start to pyrolyse, char formation also starts; however, the char fraction is small, and so the oxygen flux required is small, indi-

cating that not enough char is present for oxidation and thus the process is kinetically controlled.

Further downstream char is available (and hence the required oxygen mass flux is high) but oxygen is practically not available, hence the process here is oxygen diffusion controlled. In fact, most of the char oxidation happens in this regime when oxygen reaches the surface. Lastly there is again a kinetically controlled regime where the char oxidation rate falls because of reduced available char and a drop in temperature. At the point char oxidation stops CO_2 concentration also drops. This can be seen in Fig. 22b. Increasing pre-exponential factor in the char-oxidation rate therefore increases (Fig. 21b–d) char oxidation in pine needle to proceed via oxygen diffusion limited process.

10. Conclusion

A detailed numerical model has been developed to predict opposed flame spread phenomena over thin cylindrical charring fuels considering oxidation of char. Coordinated and detailed experimental measurements on downward flame spread over a pine needle were used to compare and validate the numerical model. The kinetic parameters for combustion and pyrolysis were calibrated using experimental downward flame spread rate data and blow-off extinction opposed flow velocity. The calibrated model predictions of detailed flame structure compared quite well with those obtained from the experiments. In addition to establishing the model, several interesting features related to influence of char and its oxidation in the flame spread process were revealed. These can be summarized as follows.

For thin fuels, char formation strongly influences the flame spread rate. The influence of char to decrease the flame spread rate was primarily due to the way formation of char is accounted. Char formation simultaneously with pyrolysate upon pyrolysis of virgin fuel had a much higher influence than char formation in a staged fashion. This was found to be due to significantly lower fuel vapour mass distribution near the flame leading edge compared to the staged char model.

Char oxidation was found to occur a few millimetres downstream of the end of the pyrolysis zone due to lack of oxygen at the fuel surface in the immediate vicinity of the flame leading edge. In this region, atmospheric oxygen is consumed by the combustion of pyrolysate. This is confirmed in both experiments and simulations. This distance decreases with increase in opposed flow velocity.

Char oxidation for thin fuels is influenced by char oxidation kinetics and the oxygen diffusion rate. However, oxygen diffusion rate mostly determines the char oxidation rate. Char oxidation kinetics limit the overall rate at the flame leading edge and in regions further downstream.

Acknowledgment

The authors acknowledge funding from Joint RSF/DST Grant 16-49-02017 and DST/INT/RUS/RSF/P-16.

Appendix A

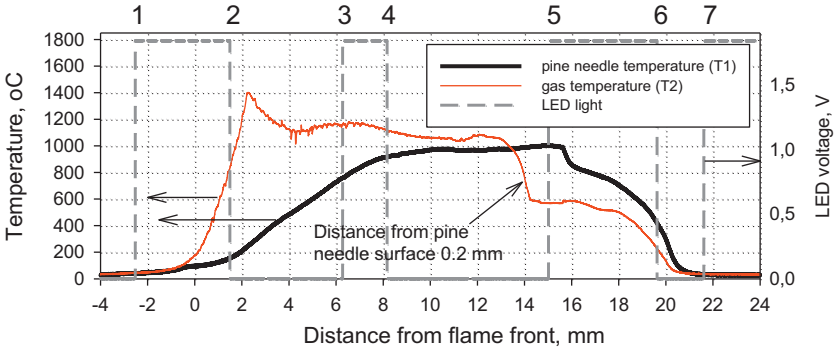

Fig. A1. Temperature profiles in gas phase at 0.2 mm perpendicular to the pine needle surface and condensed phase (center of pine needle) for a downward spreading flame over a single pine needle [19].

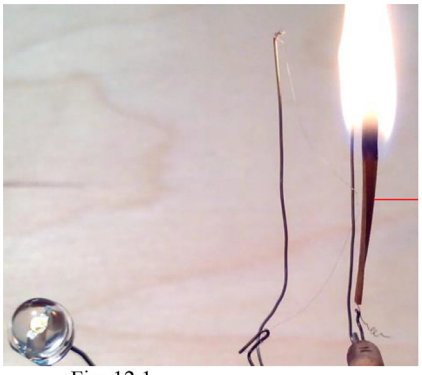
Fig. 12.1

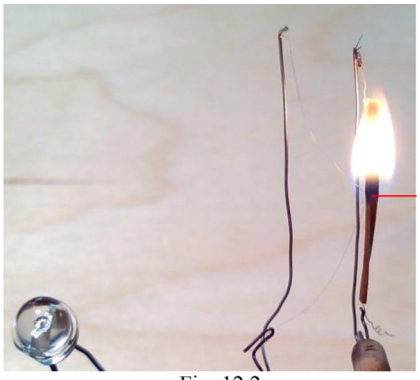
Fig. 12.2

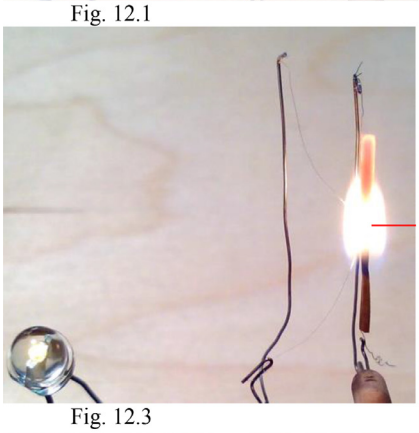
Fig. 12.3

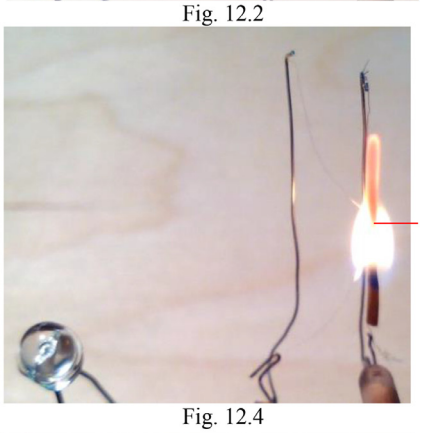
Fig. 12.4

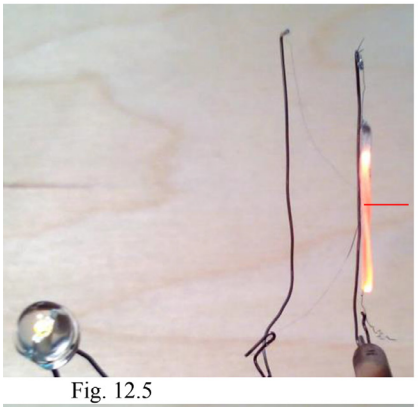
Fig. 12.5

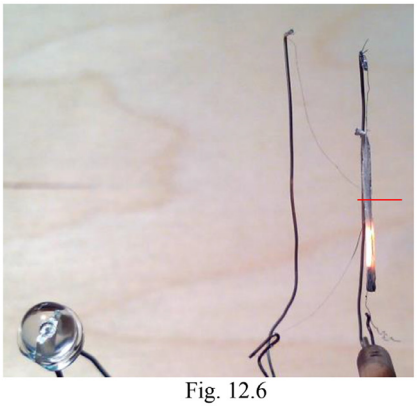
Fig. 12.6

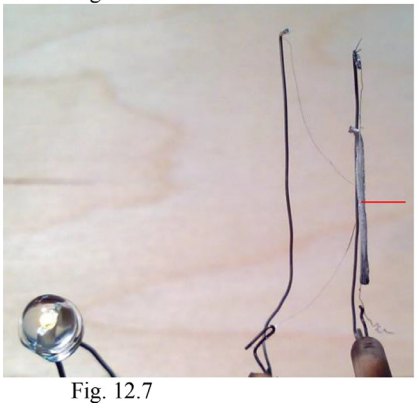
Fig. 12.7

Fig. A2. Instantaneous pictures (a–g) of downward flame spread over a single pine needle of length 20 mm [19]. These various instants during the flame spread process are at times of LED switch on or off indicated by points 1–7 respectively in Fig. A1.

References

[1] M. Vogel, F.A. Williams, Flame propagation along matchstick arrays, Cornbust. Sci. Tech. 1 (1970) 429–436.
[2] G.F. Carrier, F.E. Fendell, P.S. Feldman, Wind-aided flame spread along a horizontal fuel slab, Combust. Sci. Tech. 23 (1980) 41–78.
[3] G.F. Carrier, F.E. Fendell, S. Fink, Towards wind-aided flame spread long a horizontal charring slab: the steady flow problem, Combust. Sci. Tech. 32 (1983) 161–209.
[4] I.S. Wichman, A. Atreya, Simplified model for the pyrolysis of charring materials, Combust. Flame 68 (3) (1987) 231–247.
[5] C. Di Blasi, S. Crescitelli, G. Russo, Model of the flow assisted spread of flames over a thin charring combustible, Proc. Combust. Inst. 22 (1988) 1205–1212.
[6] C. Di Blasi, Processes of flames spreading over the surface of charring fuels: effects of the solid thickness, Combust. Flame 97 (1994) 225–239.
[7] A. Atreya, A model of opposed-flow flame spread over charring materials, Proc. Combust. Inst. 29 (2002) 227–236.
[8] W.C. Park, A. Atreya, H.R. Baum, Experimental and theoretical investigation of heat and mass transfer processes during wood pyrolysis, Combust. Flame 157 (2010) 481–494.
[9] Y. Nakamura, H. Yamashita, T. Takeno, G. Kushida, Effects of gravity and ambient oxygen on a gas-phase ignition over a heated solid fuel, Combust. Flame 120 (2000) 34–48.
[10] Y. Nakamura, T. Kashiwagi, K.B. Mcgrattan, H.R. Baum, Enclosure effects on flame spread over solid fuels in microgravity, Combust. Flame 130 (2002) 307–321.
[11] O.P. Korobeinichev, A.G. Tereshchenko, A.A. Paletsky, A.G. Shmakov, M.B. Gonchikzhapov, D. Bezmaternykh, L.Yu Kataeva, D.A. Maslennikov, N. Liu, The velocity and structure flame front at spread of fire across the pine needle bed: Experiment, Advances in forest fire research, Imprensa da Universidade de Coimbra, Coimbra, Portugal, 2014, pp. 451–458. doi: 10.14195/978-989-26-0884-6_52.
[12] C.Sanchez Tarifa, G. Corchero, G.L. Just, An Experimental Programme on Flame Spread in Reduced Gravity Conditions, Appl. Micrograv. tech. I (1988) 4.
[13] M.F. Bundy, A computational model for flame spread along cylindrical fuels in a microgravity environment, Washington State University, 1998.
[14] A.E. Abulbaida, Experimental study of downward flame spread rate on PMMA, Dalhousie University, 2014.
[15] O. Fujita, M. Kikuchi, K. Ito, K. Nishizawa, Effective mechanisms to determine flame spread rate over ethylene-tetrafluoroethylene wire insulation: Discussion on dilution gas effect based on temperature measurements, Proc. Combust. Inst. 28 (2000) 2905–2911.
[16] S.L. Olson, P.V. Ferkul, Microgravity flammability boundary for PMMA rods in axial stagnation flow: Experimental results and energy balance analyses, Combust. Flame 180 (2017) 217–229.
[17] S. Bhattachaijee, R. Worley, R.A. Altenkirch, M. Bundy, L. Tang, M. Delichatsios, and K. Sacksteder, “Opposed-Flow Flame Spread over Cylindrical Fuels”, Proceedings of the 1997 Technical Meeting of the Central States Section of the Combustion Institute.
[18] F.J. Higuera, A. Linan, Flame spread along a fuel rod in the absence of gravity, Combust. Theory Model. 3 (1999) 259–265.
[19] O.P. Korobeinichev, A.G. Shmakov, K.N. Osipova, A. Kumar, K. Naresh, Experimental study and numerical modeling of downward flame spread along a single pine needle: Part 1 (Experiments), Combust. Sci. Tech. 190 (2018) 164–185.
[20] M.D. Smooke, V. Giovangigli, Formulation of the premixed and non premixed test problem, Lecture Notes in Physics, Series 384, Chapter 1, Spring-Verlag, NewYork, 1991.
[21] P.L. Walker Jr., F.J. Rusinko, L.G. Austin, Gas Reactions of Carbon, Adv. Catalysis 11 (1959) 133–221.
[22] D. Gray, J.G. Cogoli, R.H. Essenhigh, Problems in Pulverized Coal and Char Combustion, Adv. Chem. Series 132 (1976) 72–91.
[23] K.L. Smith, L.D. Smoot, T.H. Fletcher, R.J. Pugmire, The structure and reaction processes of coal, Plenum Press, New York, 1994.
[24] M.N. Kiran Kumar, A. Kumar, The dynamics of near limit self-propagating flame over thin solid fuels in microgravity, Proc. Combust. Inst. 36 (2017) 3081–3087.
[25] V. Malhotra, C. Kumar, A. Kumar, Opposed flow flame spread over an array of thin solid fuel sheets in microgravity environment, Combust. Theory Model. 17 (5) (2013) 837–857.
[26] A. Kumar, H.Y. Shih, J.S. T'ien, A comparison of extinction limits and spreading rates in opposed and concurrent spreading flames over thin solids, Combust. Flame 132 (2003) 667–677.
[27] C.L Tien, Thermal radiation properties of gases, Advances in Heat Transfer, Vol. 5, Academic Press, New York, 1968, pp. 234–254.
[28] C. Kumar, A. Kumar, On the role of radiation and dimensionality in predicting flow opposed flame spread over thin fuels, Combust. Theory Model. 16 (3) (2012) 537–569.
[29] J.L. Rhatigan, H. Bedir, J.S. T'ien, Gas Phase Radiative Effects on the Burning and Extinction of a Solid, Combustion and Flame 112 (1998) 231–241.
[30] K. Chenthil, Some Numerical Investigations on Opposed Flow Flame Spread over Thin Solid Fuels, Indian Institute of Technology, Madras, 2012.
[31] O.P. Korobeinichev, A.G., Tereshchenko, A.A Paletsky, M.B. Gonchikzhapov, I.K. Shundrina, D.A. Maslennikovd, Y.K. Naganovsky, N. Liu, Kinetics of pine needles pyrolysis, 8th International Seminar on Flame Structure, Berlin, Germany, September 21–24.
[32] J Kleinhenz, P. Ferkul, R. Pettegrew, K.R. Sacksteder, J.S. T'ien, One sided flame spread phenomena of a thermally thin composite cotton/fiberglass fabric, Fire Mater. 29 (2005) 23–37.
[33] C. Westbrook, F. Dryer, Simplified reaction mechanisms for the oxidation of hydrocarbon fuels in flames, Combust. Sci. Technol. 27 (1981) 31–43.